Monthly Notices
of the
ROYAL ASTRONOMICAL SOCIETY

MNRAS **441,** 3524–3542 (2014) doi:10.1093/mnras/stu778

The WiggleZ Dark Energy Survey: improved distance measurements to $z = 1$ with reconstruction of the baryonic acoustic feature

Eyal A. Kazin,[1,2]★ Jun Koda,[1,2] Chris Blake,[1] Nikhil Padmanabhan,[3] Sarah Brough,[4] Matthew Colless,[4] Carlos Contreras,[1,5] Warrick Couch,[1,4] Scott Croom,[6] Darren J. Croton,[1] Tamara M. Davis,[7] Michael J. Drinkwater,[7] Karl Forster,[8] David Gilbank,[9] Mike Gladders,[10] Karl Glazebrook,[1] Ben Jelliffe,[6] Russell J. Jurek,[11] I-hui Li,[12] Barry Madore,[13] D. Christopher Martin,[8] Kevin Pimbblet,[14,15] Gregory B. Poole,[1,16] Michael Pracy,[1,6] Rob Sharp,[16,17] Emily Wisnioski,[1,18] David Woods,[19] Ted K. Wyder[8] and H. K. C. Yee[12]

Affiliations are listed at the end of the paper

Accepted 2014 April 17. Received 2014 March 14; in original form 2013 December 31

ABSTRACT

We present significant improvements in cosmic distance measurements from the WiggleZ Dark Energy Survey, achieved by applying the reconstruction of the baryonic acoustic feature technique. We show using both data and simulations that the reconstruction technique can often be effective despite patchiness of the survey, significant edge effects and shot-noise. We investigate three redshift bins in the redshift range $0.2 < z < 1$, and in all three find improvement after reconstruction in the detection of the baryonic acoustic feature and its usage as a standard ruler. We measure model-independent distance measures $D_V(r_s^{fid}/r_s)$ of 1716 ± 83, 2221 ± 101, 2516 ± 86 Mpc (68 per cent CL) at effective redshifts $z = 0.44$, 0.6, 0.73, respectively, where D_V is the volume-averaged distance, and r_s is the sound horizon at the end of the baryon drag epoch. These significantly improved 4.8, 4.5 and 3.4 per cent accuracy measurements are equivalent to those expected from surveys with up to 2.5 times the volume of WiggleZ without reconstruction applied. These measurements are fully consistent with cosmologies allowed by the analyses of the Planck Collaboration and the Sloan Digital Sky Survey. We provide the $D_V(r_s^{fid}/r_s)$ posterior probability distributions and their covariances. When combining these measurements with temperature fluctuations measurements of *Planck*, the polarization of *Wilkinson Microwave Anisotropy Probe* 9, and the 6dF Galaxy Survey baryonic acoustic feature, we do not detect deviations from a flat Λ cold dark matter (ΛCDM) model. Assuming this model, we constrain the current expansion rate to $H_0 = 67.15 \pm 0.98$ km s^{-1}Mpc^{-1}. Allowing the equation of state of dark energy to vary, we obtain $w_{DE} = -1.080 \pm 0.135$. When assuming a curved ΛCDM model we obtain a curvature value of $\Omega_K = -0.0043 \pm 0.0047$.

Key words: cosmological parameters – distance scale – large-scale structure of the universe.

1 INTRODUCTION

The baryonic acoustic feature is regarded as a reliable tool for measuring distances, which can be used to probe cosmic expansion rates and hence assist in understanding the mysterious nature of the recent cosmic acceleration (Riess et al. 1998; Perlmutter et al. 1999; Blake & Glazebrook 2003; Seo & Eisenstein 2003). Early plasma-photon acoustic waves that came to a near-stop at a redshift $z \sim 1100$ left these baryonic signatures imprinted at a comoving radius of ∼150 Mpc in both the cosmic microwave background (CMB) temperature fluctuations and in the distribution of matter, as an enhancement in the clustering amplitude of overdensities at this 'standard ruler' distance (Peebles & Yu 1970).

However, the signature in the distribution of matter, and hence in galaxies, experienced a damping due to long-range coherent bulk

★E-mail: eyalkazin@gmail.com

motions generated by tidal gravitational forces. In the linear density field, galaxies coherently move by ∼5 Mpc from their original positions, which causes smoothing of the otherwise sharp feature at the scale of 150 Mpc in the clustering correlation function. Although this damping is well understood and modelled (Meiksin, White & Peacock 1999; Seo & Eisenstein 2007; Angulo et al. 2008; Crocce & Scoccimarro 2008; Sánchez, Baugh & Angulo 2008; Seo et al. 2008; Smith, Scoccimarro & Sheth 2008; Kim et al. 2009), it decreases the accuracy with which the feature may be used as a standard ruler.

To correct for the effects of large-scale motions, Eisenstein et al. (2007) suggested the method of reconstruction of the baryonic acoustic feature. By using the density field to infer the displacements caused by these bulk flows in linear theory, one can retract the galaxies to their near-original positions, and hence sharpen the baryonic acoustic signature. They concluded that this method improves the usage of the baryonic acoustic feature as a standard ruler. The technique has since been further developed, showing that this procedure minimizes the systematic errors in the bias of geometric information obtained from matter and galaxies (Noh, White & Padmanabhan 2009; Padmanabhan, White & Cohn 2009; Seo et al. 2010; Mehta et al. 2011). Mehta et al. (2011) concluded that distance measurements made when using galaxies with a low galaxy to matter density bias of $b = \delta_{\rm gal}/\delta_{\rm m} \sim 1$, such as those analysed here, have a low systematic error of ∼0.2–0.25 per cent which is reduced to 0.1–0.15 per cent when applying reconstruction (see their fig. 5).

The first successful application of the technique to galaxy data was reported by Padmanabhan et al. (2012), who improved the distance constraint to $z = 0.35$ by sharpening the baryonic acoustic feature of the luminous red galaxy sample (Eisenstein et al. 2001) of the SDSS-II (York et al. 2000). Testing realistic mock catalogues, they showed that the technique yields unbiased improved results. A further application of the technique was performed by the SDSS-III Baryon Oscillation Spectroscopic Survey (BOSS) using a massive galaxy sample at $z = 0.57$ (Anderson et al. 2012, 2014b). The inability of the technique to improve constraints in this particular case may be attributed to sample variance in the sense that the pre-reconstruction measurement was on the fortunate side of expectations (Kazin et al. 2013). Recently the BOSS Collaboration have shown this to be the mostly likely explanation, by showing improvement of distance measures when probing galaxy samples two and three times as large (Anderson et al. 2014a, see their fig. 4.)

In this study, we apply the reconstruction technique to galaxies mapped by the WiggleZ Dark Energy Survey (Drinkwater et al. 2010). The $0.2 < z < 1$ range of WiggleZ enables the survey to probe dark energy at a unique effective redshift of $z = 0.73$, which is close to the beginning of the acceleration phase, according to the dark energy cold dark matter (CDM) paradigm. We have previously reported measurements using the baryonic acoustic feature in this redshift range with accuracies of ∼4.5–7.5 per cent (Blake et al. 2011). In this analysis, we show that reconstruction improves the detectability of the baryonic acoustic feature and yields *substantially* tighter distance constraints.

When applying reconstruction to WiggleZ we are confronted by various challenges compared to other galaxy surveys. The WiggleZ volumes are patchy with substantial edge effects, because each survey region is only ∼500 h^{-1}Mpc in dimension with additional incompleteness due to the input catalogues. In addition, clustering measurements using the highest redshifts of the volume also contain fairly high shot-noise corresponding to $nP \sim 1$, where n is the number density and P is the characteristic power spectrum amplitude at wavenumber $k \sim 0.15\,h$ Mpc^{-1}. Hence, we are required to test if reconstruction of the density fields of such volumes could potentially cause possible biases when displacing the galaxies.

To test for this, we apply the algorithm to a myriad of realistic simulated realizations. Constructing mock catalogues from N-body simulations for WiggleZ is a challenging problem because the galaxies trace dark matter haloes with masses $\sim 10^{12}\,h^{-1}\,{\rm M}_{\odot}$, an order of magnitude lower than those populated by luminous red galaxies. For this reason, in past analyses of WiggleZ (e.g. Blake et al. 2011) we used log-normal realizations to support the data analysis (e.g. to determine the covariance of the measurement). These, however, do not contain realistic displacement information. Hence, to support this study we generated 600 mock realizations based on a more accurate Lagrangian comoving scheme, as described in Section 2.2.

Another difference between the past and current WiggleZ analyses is the manner in which we model the correlation function ξ. In past analyses, we modelled the full shape, resulting in model-dependent measurements. The reason for this is that when assuming a theoretical model for ξ its full shape may be used as a standard ruler (e.g. see Eisenstein et al. 2005; Sánchez et al. 2012, 2013). As reconstruction involves smoothing of the density field, it is difficult to model the overall broad-band shape of the post-reconstruction power spectrum. For this reason, in this analysis we are only interested in the baryonic acoustic peak position, and hence focus on the geometric information. This means that we are required to marginalize over the shape information, which makes the distance measurements reported here model independent.

This study is presented as follows. In Section 2, we present the data, simulated data, the reconstruction technique and the construction of the two-point correlation functions. In Section 3, we describe the method used to calculate the geometric constraints, including the construction of the fitting model. In Section 4, we present distance measurements from the data and compare with those obtained with the simulations. This section is concluded by cosmological implications. We summarize in Section 5.

Unless otherwise stated, we assume a flat ΛCDM fiducial cosmology as defined in Komatsu et al. (2009): a dark matter density of $\Omega_{\rm m} = 0.27$, a baryon density of $\Omega_{\rm b} = 0.0448$, a spectral index of $n_{\rm s} = 0.963$, an rms of density fluctuations averaged in spheres of radii at 8 h^{-1}Mpc of $\sigma_8 = 0.8$ and $h = 0.71$, where the local expansion rate is defined as $H_0 = 100h$ kms^{-1} Mpc^{-1}.

2 DATA

2.1 Galaxy sample

The WiggleZ Dark Energy Survey (Drinkwater et al. 2010) is a large-scale galaxy redshift survey of bright emission-line galaxies over the redshift range $z < 1$, which was carried out at the Anglo-Australian Telescope between 2006 August and 2011 January. In total, of the order of 200 000 redshifts of UV-selected galaxies were obtained, covering of order 1000 deg^2 of equatorial sky. In this study, we analyse the same final WiggleZ galaxy sample as utilized by Blake et al. (2011) for the measurements of baryonic acoustic oscillations (BAOs) in the galaxy clustering pattern. After cuts to maximize the contiguity of the observations, the sample contains 158 741 galaxies divided into six survey regions – the 9-h, 11-h, 15-h, 22-h, 1-h and 3-h regions. The survey selection function within each region was determined using the methods described by Blake et al. (2012).

For purposes of this study, following the analysis of Blake et al. (2011), we divided the galaxies into three redshift bins of width $\Delta z = 0.4$, defined here as: $\Delta z^{\rm Near}$ $(0.2 < z < 0.6)$, $\Delta z^{\rm Mid}$

($0.4 < z < 0.8$) and $\Delta z^{\rm Far}$ ($0.6 < z < 1.0$). Note that the second bin fully overlaps with the other two, which are independent from each other.

Blake et al. (2011) calculated the effective redshift $z_{\rm eff}$ of ξ in each slice as the weighted mean redshift of the galaxy pairs in the separation bin $100 < s < 110\ h^{-1}$Mpc, where the z of a pair is the average $(z_1 + z_2)/2$. For $\Delta z^{\rm Near}$, $\Delta z^{\rm Mid}$ and $\Delta z^{\rm Far}$, this results in $z_{\rm eff} = 0.44$, 0.6 and 0.73, respectively.

2.2 The WiZ-COLA simulation

Simulated galaxy catalogues are a key tool for interpretation of large-scale structure measurements which are used to determine covariances, and test methodologies for potential biases. In this section, we briefly describe the construction of the mock catalogues used in this analysis. For full details, the reader is referred to Koda et al. (in preparation).

Constructing hundreds of mock catalogues from N-body simulations for WiggleZ is a challenging problem because the galaxies trace dark matter haloes with masses $\sim 10^{12}\ h^{-1}\ {\rm M}_\odot$, an order of magnitude lower than those populated by luminous red galaxies. For this reason, we employed cheaper methods of production of mocks that yield a good approximation to N-body simulations.

In our first attempt to build mock catalogues, we tried implementing the second-order Lagrangian Perturbation Theory method (Bernardeau et al. 2002), as described in Manera et al. (2013). However, we found that because of poor resolution, this method failed to identify correctly low-mass haloes such as those in which the low-bias WiggleZ galaxies reside.

For this reason, we developed a parallel version of the COmoving Lagrangian Acceleration simulation (COLA; Tassev, Zaldarriaga & Eisenstein 2013) which we used to generate 3600 realizations of 10-time step simulations – 600 realizations for each of the six observational regions in the WiggleZ survey.

Each of the WiggleZ COLA (WiZ-COLA) simulations consists of 1296^3 N-body particles in a box of $600\ h^{-1}$ Mpc on a side, which gives a particle mass of $7.5 \times 10^9\ h^{-1}\ {\rm M}_\odot$. We use 3×1296 grids per dimension to calculate the gravitational force with enough spatial resolution (Tassev et al. 2013). This simulation configuration has sufficient volume to contain one region of the WiggleZ survey for each redshift range $z = 0.2$–0.6, 0.4–0.8 or 0.6–1.0, and simultaneously resolves dark matter haloes down to $10^{12}\ h^{-1}\ {\rm M}_\odot$, which host emission-line galaxies observed in the WiggleZ survey. Each simulation takes 15 min with 216 computation cores, including halo finding.

As fully described in Koda et al. (in preparation), we populate the haloes using a Gaussian halo occupation distribution, such that the resulting projected correlation functions $w_{\rm p}(r_{\rm p})$ match those of the observations.

We then apply the WiggleZ selection function to the mock galaxies to make simulated catalogues with correct survey geometry. When we apply the mask, we rotate the simulation box to fit the survey volume into the box with minimum overlap, using the remapping algorithm by Carlson & White (2010) to find the best rotation. We output three snapshots at $z = 0.44$, 0.6 and 0.73, for the three redshift bins, $\Delta z^{\rm Near}$, $\Delta z^{\rm Mid}$ and $\Delta z^{\rm Far}$, respectively. In each redshift bin, we use the appropriate independent 600 mocks to generate covariance matrices, as described in Sections 2.4 and 3.2, and analyse each redshift bin separately to measure $D_{\rm V}/r_{\rm s}$ (as defined below).

Our simulation box is large enough for one redshift bin, but not for the full range $0.2 < z < 1$. This is not a problem when we treat different redshifts separately (Sections 4.1 and 4.2), but does not give the correct correlation between $\Delta z^{\rm Mid}$ and the other two redshift bins. For this reason, we also create 300 additional mock catalogues for each of the six regions to evaluate the correlation coefficient between the $D_{\rm V}/r_{\rm s}$ measurements in the overlapping redshift regions (as presented in Section 4.5). We combine, or *stitch*, two mock catalogues from different realizations of $z = 0.2$–0.6 and $z = 0.6$–1.0, by joining them together at their sharp edges of $z = 0.6$ and cut out the redshift region $z = 0.4$–0.8 appropriately from each. This mock does not have accurate clustering across the boundary at $z = 0.6$, but contains the same mock galaxies that exist in the other two redshift regions 0.2–0.6 and 0.6–1.0, which is necessary to compute the correlation between the overlapping redshift data. Because for each of the 600 realizations we use different snapshots to create the three original Δz volumes, by stitching $\Delta z^{\rm Near}$ and $\Delta z^{\rm Far}$ from different realizations we end up with 300 stitched versions.

2.3 Reconstruction of the density field

In order to reduce effects of large-scale coherent motions on the baryonic acoustic feature, the reconstruction of the density field method is applied by shifting the galaxies to their near-original positions in the linear density field. Here, we describe the calculation of the displacement vectors from the density fields, including the survey selection effects.

We determine the displacement field $\mathbf{\Psi}$ within the Zel'dovich approximation (Zel'dovich 1970) following the method described by Padmanabhan et al. (2012). Given that large-scale structure outside the survey regions contributes gravitationally to displacements within, it is necessary to enclose the observed volume within a larger 'embedded' volume, into which we must extrapolate the density field in a statistically consistent manner. The extrapolation is over any unobserved regions inside the survey cone, and into a 'padding' volume which extends $200\ h^{-1}$ Mpc beyond each edge of a cuboid enclosing the survey region. For each of the 18 volumes analysed (6 angular regions and 3 redshift slices), we apply the reconstruction technique described here independently, because we do not expect volumes to affect each other due to the large distances between them.

We summarize the steps of the method as follows, distinguishing between quantities evaluated over the observed and embedded volumes.

(i) We evaluate the smoothed, observed galaxy overdensity field, $\delta(\boldsymbol{x})$, in each survey region. We carry out this calculation by binning the galaxy distribution and normalized selection function in a 3D comoving coordinate grid with a cell size of $5\ h^{-1}$Mpc on the side, denoting these gridded distributions as $D_{\rm c}$ and $R_{\rm c}$ (where c is the cell number), and then determining δ by smoothing these distributions with a Gaussian kernel $G(\boldsymbol{x}) = {\rm e}^{-(\boldsymbol{x}\cdot\boldsymbol{x})/2\lambda^2}$ such that $\delta_{\rm c} = {\rm smooth}(D_{\rm c})/{\rm smooth}(R_{\rm c}) - 1$ and $\langle\delta_{\rm c}\rangle = 0$. We choose an rms smoothing scaling $\lambda = 15\ h^{-1}$Mpc for our analysis, noting that our results are not sensitive to this choice. From here on we drop the 'c' notation from δ, for convenience.

(ii) We generate a realization of an 'unconstrained' Gaussian random field across the embedded volume, $\tilde{\delta}_U$, using an assumed galaxy power spectrum $P(k)$ consistent with fits to the data in the observed region. We smooth the unconstrained overdensity field in the same manner as the observed overdensity field.

(iii) We use the Hoffman–Ribak algorithm (Hoffman & Ribak 1991; equation 3 in Padmanabhan et al. 2012), as our best estimate of the overdensity field in the embedded volume:

$$\tilde{\delta} = \tilde{\delta}_U + \tilde{\mathbf{C}}\,\mathbf{C}^{-1}(\delta - \mathbf{P}\tilde{\delta}_U), \tag{1}$$

where $\mathbf{P}$ is a matrix of zeros and ones which projects a vector from the embedded volume to the observed volume, and $\mathbf{C}$ and $\tilde{\mathbf{C}}$ are the covariance matrices of pixels in the observed and embedded volumes, respectively, which are just the correlation functions ξ:

$$C_{ij} = \langle \delta(\boldsymbol{x}_i)\,\delta(\boldsymbol{x}_j)\rangle = \xi(|\boldsymbol{x}_i - \boldsymbol{x}_j|). \tag{2}$$

Following Padmanabhan et al. (2012), we solve equation (1) in a number of steps. (i) We evaluate $u = \delta - \mathbf{P}\tilde{\delta}_U$ by simple projection of $\tilde{\delta}_U$ from the embedded to the observed volumes. (ii) We solve $v = \mathbf{C}^{-1}u$ using a preconditioned conjugate gradient algorithm to determine the solution of $\mathbf{C}v = u$, using a modified version of the Numerical Recipes subroutine `linbcg`. For each iteration, the expression $\mathbf{C}v$ is evaluated by fast Fourier transforms, using the fact that multiplication by $\mathbf{C}$ is equivalent to convolution by $\xi(r)$. Therefore, FT($\mathbf{C}v$) is equal to the product of $P(k)$ and FT(v), where we note that the power spectra contain the galaxy shot-noise contribution $1/n$ in terms of mean galaxy density n. (iii) We project v into the embedded space, $\tilde{v} = \mathbf{P}^{-1}v$, and calculate $\tilde{w} = \tilde{\mathbf{C}}\tilde{v}$ as above. (iv) The final overdensity field in the embedded volume is given by $\tilde{\delta} = \tilde{\delta}_U + \tilde{w}$.

(iv) Finally, we estimate the displacement field $\boldsymbol{\Psi}$ in the Zel'dovich approximation as

$$\boldsymbol{\nabla}\cdot\boldsymbol{\Psi} + (f/b)\,\boldsymbol{\nabla}\cdot(\Psi_s\hat{\boldsymbol{s}}) = -\tilde{\delta}/b, \tag{3}$$

where f is the growth rate of structure at the survey redshift, b is the galaxy bias factor and $\Psi_s = \boldsymbol{\Psi}\cdot\hat{\boldsymbol{s}}$ is the displacement in the line-of-sight direction. We assume values $f = 0.70\,(z = 0.44)$, $0.76\,(z = 0.6)$, $0.79\,(z = 0.73)$ and $b = 1,\ 1.1,\ 1.2$ (for $\Delta z^{\rm Near}$, $\Delta z^{\rm Mid}$ and $\Delta z^{\rm Far}$, respectively), noting that our results are not sensitive to these choices. The flat-sky approximation is valid for the WiggleZ survey regions, and we can therefore take the line-of-sight direction as parallel to a single Cartesian axis, which we take as the x-direction, such that $\Psi_s = \boldsymbol{\Psi}\cdot\hat{\boldsymbol{x}}$. We then solve equation (3) by substituting $\boldsymbol{\Psi} = \boldsymbol{\nabla}\phi$ and taking the Fourier transform of the equation to obtain

$$\left[(1 + f/b)k_x^2 + k_y^2 + k_z^2\right]\mathrm{FT}[\phi](k_x, k_y, k_z) = \frac{\mathrm{FT}[\tilde{\delta}](k_x, k_y, k_z)}{b}, \tag{4}$$

where FT is the Fourier transform.

The inverse Fourier transform then yields the displacement field $\boldsymbol{\Psi}(x, y, z) = \boldsymbol{\nabla}\phi$.

(v) We then shift each galaxy and random point by $-\boldsymbol{\Psi}$. To subtract the Kaiser effect in redshift space, the galaxies are also shifted an additional $-f\Psi_x$ in the x dimension. This additional shift is not applied to the random points.

At the end of this procedure, for each of the 18 volumes, we obtain a shifted data catalogue and a shifted random point catalogue.

2.4 Correlation functions

To estimate the correlation function, we compare pair counts of the data to those of a sample of random points. The random points are distributed in a Poisson-like manner, such that they trace the mask of the survey, as described in Blake et al. (2012). To reduce shot-noise effects of the mask, we use a ratio of 100 random points per data point.

Before calculating pairs, we first convert the data and randoms from the R.A, Dec., z coordinate system to a comoving Euclidian system assuming a flat ΛCDM fiducial cosmology as defined in Komatsu et al. (2009): $\Omega_{\rm m} = 0.27$. When calculating the pairs, each galaxy and random point is assigned a weight according to the Feldman, Kaiser & Peacock (1994) minimum variance weighting, which takes into account the number density at a given redshift $n(z)$:

$$w(z) = \frac{1}{1 + P\cdot n(z)}, \tag{5}$$

where we assume $P = 5000\,h^{-3}$ Mpc^3 as the characteristic power spectrum amplitude at the physical scales of interest.

We calculate the Landy & Szalay (1993) correlation function estimator ξ for each of the 18 volumes. This is done first by calculating:

$$\xi(\mu, s) = \frac{DD - 2DR + RR^{\rm num}}{RR^{\rm denom}}, \tag{6}$$

where the line-of-sight direction $\mu = 1$ is defined as the direction which bisects the separation vector $\boldsymbol{s}$ between each pair, and $s \equiv |\boldsymbol{s}|$. The normalized galaxy–galaxy pair count is $DD(\mu, s)$ and similarly for the normalized galaxy–random DR and normalized random–random RR counts.

The reconstruction procedure described in Section 2.3 results in various data and random sets which we use as follows. For the pre-reconstruction case, we use the original data and random point counts where both RR terms in equation (6) are the same. In the reconstruction case, we use the shifted data for DD and DR, and shifted randoms for DR and $RR^{\rm num}$. Finally, for the $RR^{\rm denom}$ term, we use the original non-shifted randoms. In this study, we examine results using two different separation bin widths Δs, of 3.3 h^{-1}Mpc and 6.7 h^{-1}Mpc.

To account for the volume limitation of each region, the integral constraint correction is calculated as

$$I.C = \frac{\sum_{s_i}\xi^{\rm theory}(s_i)RR^{\rm num}(s_i)}{\sum_{s_i}RR^{\rm num}(s_i)} \tag{7}$$

and added to $\xi(\mu, s)$. For this purpose, the RR terms used are calculated in each region to a large separation s at which RR is zero. In the largest region, this is just over 1 h^{-1}Gpc. The theoretical model used, $\xi^{\rm theory}$, is a combination of the template used in the analysis for $s > 50$ h^{-1}Mpc (see Section 3.1), and a linear model for lower separation bins s_i. For the reconstruction case, we use the shifted random point count RR, and do not include the Kaiser boost term in $\xi^{\rm theory}$. We verify that the resulting values of $I.C$ are not sensitive to details of this procedure.

We then obtain the angle-averaged correlation function ξ_0 and quadrupole ξ_2 of each of the 18 volumes by integrating each $\xi(\mu, s)$ using the appropriate Legendre polynomials. We follow this procedure for both the data and the 600 mock catalogues, performing measurements before and after reconstruction.

To calculate the three redshift slice correlation functions $\xi^{\Delta z}$, we combine the correlation functions of six angular regions Ω in the following manner. To account for the correlations between the multipoles (Taruya, Saito & Nishimichi 2011; Kazin, Sánchez & Blanton 2012), we define the vector $\boldsymbol{\xi}^{\Omega}_{[0,2]}$ that contains ξ^{Ω}_0 and ξ^{Ω}_2 and therefore has a length equal to double the number of bins. We emphasize that we use the ξ^{Ω}_2 information to construct the $\xi^{\Delta z}_0$ because the multipoles are not independent, as shown below.

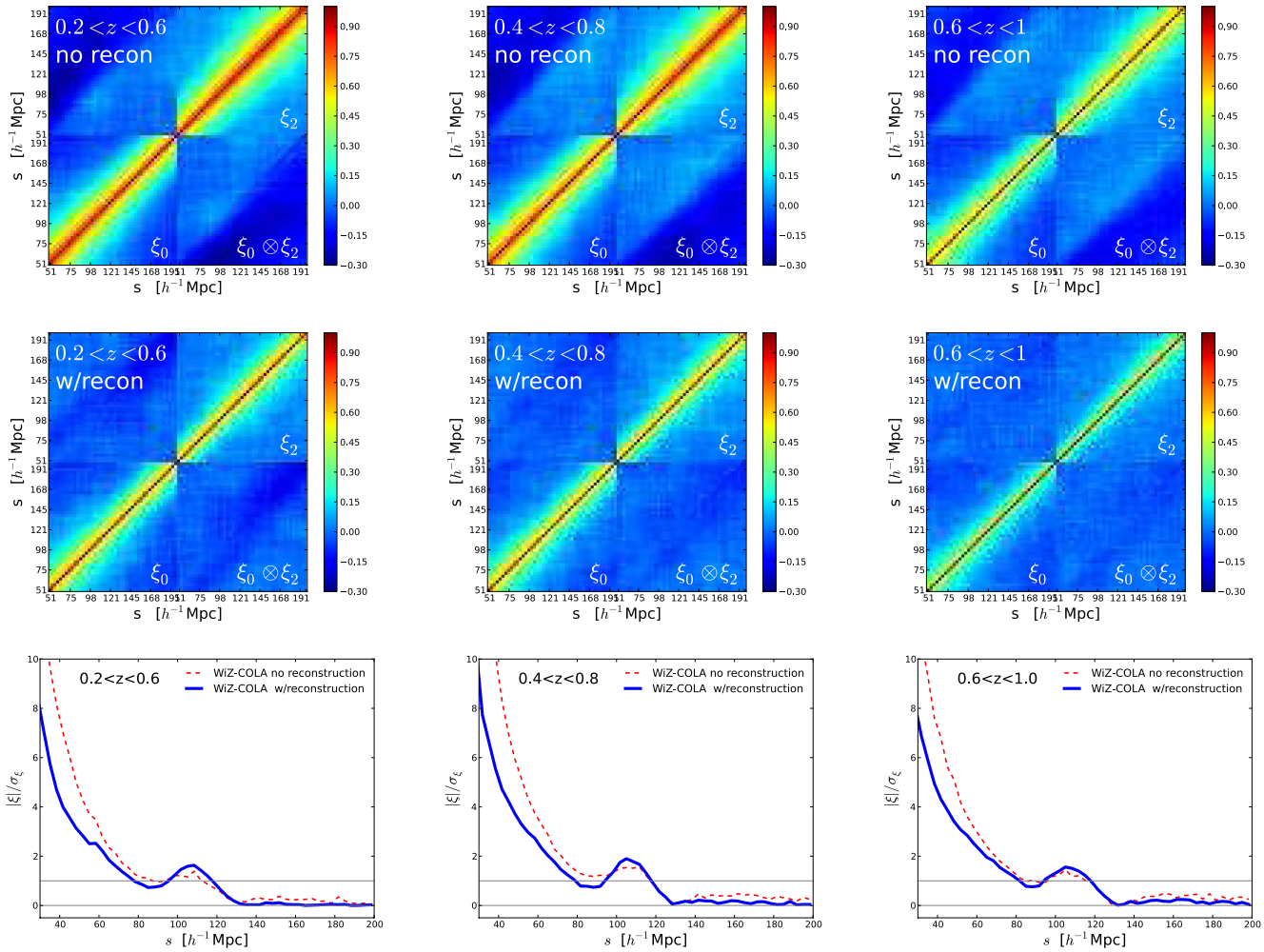

Figure 1. The top and centre panels show the normalized covariance matrix $C^{ij}_{[0,2]}/\sqrt{C^{ii}_{[0,2]}C^{jj}_{[0,2]}}$ before and after reconstruction, respectively, for each of the Δz volumes, as indicated. The bottom panels show comparisons of S/N ratios of the monopole $|\xi_0|/\sigma_{\xi_0}$, before (dashed red) and after reconstruction (solid blue), where we define the uncertainties $\sigma_{\xi_0} = \sqrt{C_{ii}}$ of the '0' component.

The resulting covariance matrix $\mathbf{C}_{[0,2]}$ is defined as

$$C^{\Omega}_{[0,2]_{ij}} = \frac{1}{N_{\rm mocks}-1}\sum_{m=1}^{N_{\rm mocks}} \left(\overline{\xi^{\Omega}_{[0,2]_i}} - \xi^{\Omega\ m}_{[0,2]\ i}\right)\left(\overline{\xi^{\Omega}_{[0,2]_j}} - \xi^{\Omega\ m}_{[0,2]\ j}\right), \quad (8)$$

where the over-line denotes the mean value of $N_{\rm mocks} = 600$.

Following White et al. (2011), we then combine these to obtain

$$\boldsymbol{\xi}^{\Delta z}_{[0,2]} = \mathbf{C}^{\Delta z}_{[0,2]} \sum_{\Omega} \left(\mathbf{C}^{\Omega}_{[0,2]}\right)^{-1} \boldsymbol{\xi}^{\Omega}_{[0,2]}, \quad (9)$$

where

$$\left(\mathbf{C}^{\Delta z}_{[0,2]}\right)^{-1} = \sum_{\Omega} \left(\mathbf{C}^{\Omega}_{[0,2]}\right)^{-1}. \quad (10)$$

Fig. 1 displays the resulting $\mathbf{C}^{\Delta z}_{[0,2]}$ for all three redshift volumes. The top and centre row of panels show the normalized values pre- and post-reconstruction, respectively. The bottom row of panels displays the signal-to-noise (S/N) of the monopole defined as $|\xi_0|/\sigma_{\xi_0}$, where the uncertainty σ_{ξ_0} is the square root of the diagonal elements of the monopole component of $\mathbf{C}_{[0,2]}$.

We notice that the off-diagonal normalized terms in the ξ_0 and ξ_2 quadrants are suppressed in the post-reconstruction case compared to pre-reconstruction. This can be explained by the restoration of the linear density field and removal of the galaxy displacements.

The bottom panels of Fig. 1 show clear improvement in the S/N of ξ_0 at the scale of the baryonic acoustic feature in all Δz. The improvement with reconstruction is 40 per cent for $\Delta z^{\rm Near}$, 25 per cent for $\Delta z^{\rm Mid}$ and 15−25 per cent for $\Delta z^{\rm Far}$. This is the case for both separation widths of $\Delta s = 3.3\,h^{-1}$Mpc and $6.7\,h^{-1}$Mpc. The S/N is lower at other scales ($s < 90\,h^{-1}$Mpc and $s > 130\,h^{-1}$Mpc) because of the suppression of the redshift-space clustering power.

We defer investigation of the cosmological content of ξ_2 to future studies, and from hereon refer to ξ as the angle-averaged measurement.

In Fig. 2, we display the resulting angle-averaged correlation functions ξ from equation (9) for the data pre- (red squares) and post-reconstruction (blue circles). The corresponding mean signal of the mock simulations $\overline{\xi}$ are displayed in Fig. 3.

In each of the three Δz bins, we see a sharpening of the baryonic acoustic peak both in the data and in the simulations. In Section 4.1, we quantify this sharpening, and in Section 4.2, we present the

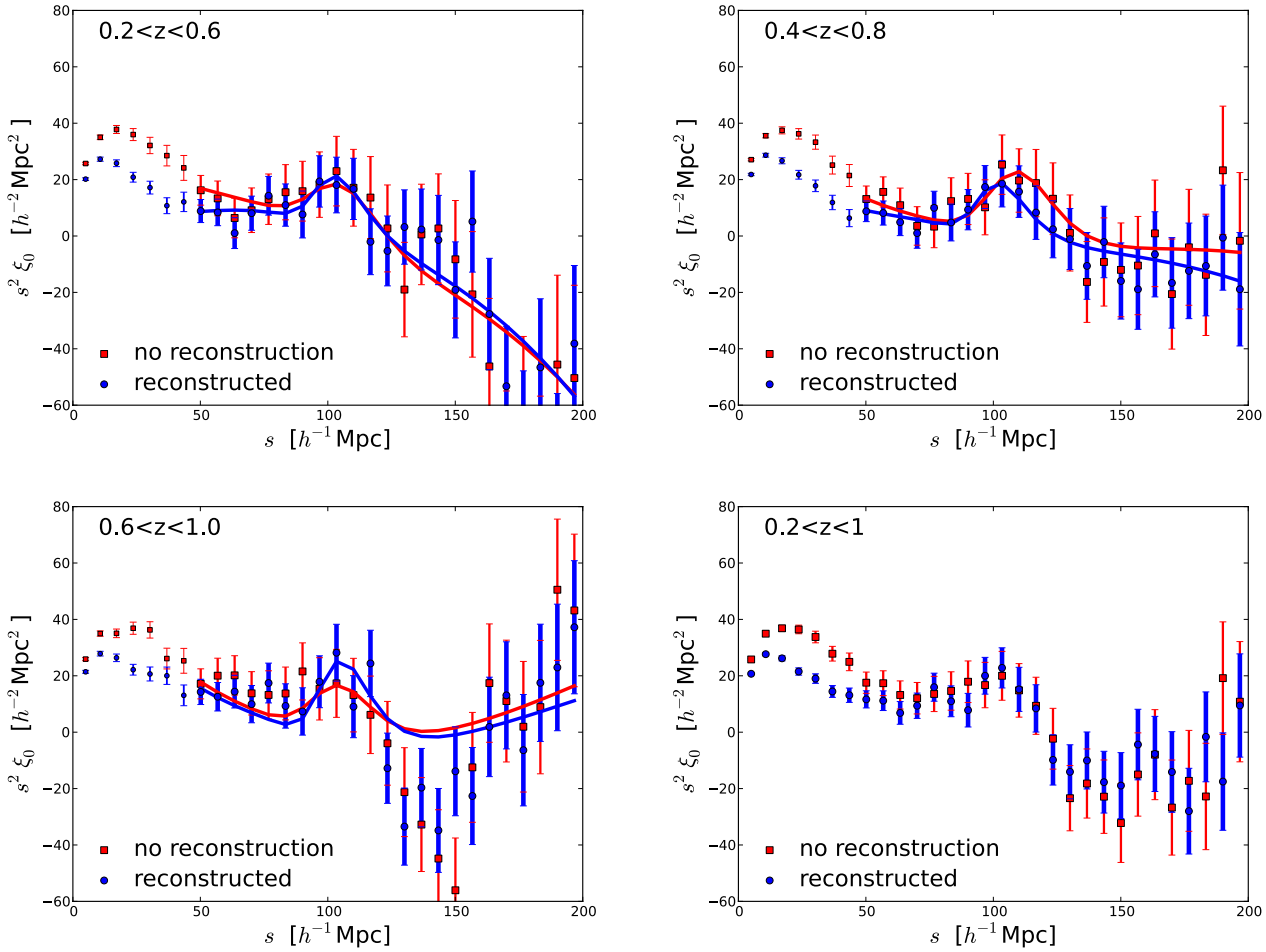

Figure 2. The WiggleZ two-point correlation functions shown before (red squares) and after applying reconstruction (blue circles) for three redshifts bins and the full z range, as indicated. These are plotted as ξs^2 to emphasize the region of the baryonic acoustic feature. The uncertainty bars are the square root of the diagonal elements of the covariance matrix. The solid lines are the best-fitting models to the range of analysis $50 < s < 200\ h^{-1}$Mpc. We see a clear sharpening of the baryonic acoustic feature after reconstruction in all cases.

improved distance measurements and compare these with expectations according to the mocks.

Comparing results pre- and post-reconstruction of the data and mocks, we also see a clear reduction post-reconstruction in the amplitude of ξ at scales outside the acoustic ring, $s < 100\ h^{-1}$Mpc and $s > 140\ h^{-1}$Mpc. This can be explained by the subtraction of the linear redshift distortions, when applying reconstruction.

The negative measurements of ξ at large scales for $\Delta z^{\rm Near}$, and the positive measurements for $\Delta z^{\rm Far}$, are consistent with the expectations of sample variance. This is best understood realizing the fact that the data points are correlated.

The various ξ and their covariance matrices can be found on the World Wide Web.[1]

3 METHODOLOGY

3.1 Modeling ξ

In our previous analysis of this data in Blake et al. (2011), we treated the full shape of ξ as a standard ruler, and modelled the whole correlation function. In our current analysis, we focus solely on the geometrical information contained in the baryonic acoustic feature $D_{\rm V}/r_{\rm s}$ (defined below) and marginalize over the information encoded in the full shape of ξ, e.g. $\Omega_{\rm m}\,h^2$ and the spectral index $n_{\rm s}$. This is because the reconstruction procedure as described in Section 2.3, while sharpening the baryonic peak and hence improving distance constraints, involves a smoothing process which affects the correlation function slope in a manner which is difficult to model.

To measure $D_{\rm V}/r_{\rm s}$ for each Δz bin, we compare the data $\xi^{\Delta z}(s_i)$ (described in Section 2.4) to a model $\xi_{\rm m}(s_i)$ defined as:

$$\xi_{\rm m}(s_{\rm f}) = a_0 \cdot \xi_{\rm T}(s_{\rm f}/\alpha) + A(s_{\rm f}), \tag{11}$$

where $\xi_{\rm T}$ is a template correlation function and $A(s)$ is a polynomial, both defined below, and $s_{\rm f}$ is the distance scale in the coordinate system of the fiducial cosmology.

As we are interested in the geometrical information encoded in the baryonic acoustic feature position, not in the full shape of ξ, we follow the procedure outlined by Xu et al. (2012) in which we marginalize over the amplitude and shape parameters a_i ($i = 0$, 1, 2, 3) as defined by

$$A(s) = a_1 + \frac{a_2}{s} + \frac{a_3}{s^2}. \tag{12}$$

[1] http://www.smp.uq.edu.au/wigglez-data/bao-random-catalogues

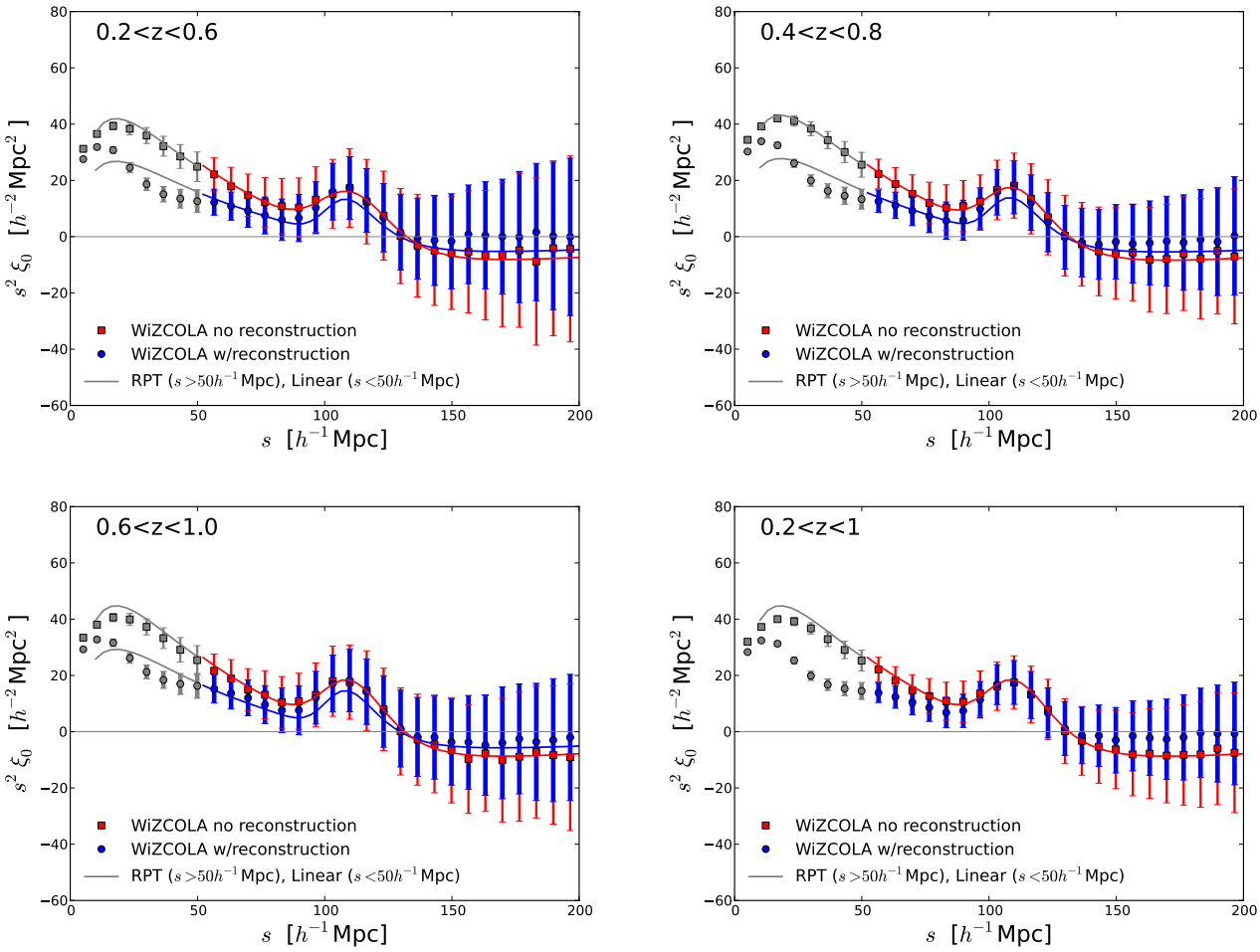

Figure 3. The mean of the simulated two-point correlation functions shown before (red squares) and after applying reconstruction (blue circles) for three redshifts bins and the full z range, as indicated. These are plotted as ξs^2 to emphasize the region of the baryonic acoustic feature. The uncertainty bars are the square root of the diagonal elements of the covariance matrix (for one WiZ-COLA realization, not the mean). The solid lines are the templates $\xi_{\rm T}$ used in the analysis (not the best-fitting model), where we focus on the range of analysis $50 < s < 200\ h^{-1}$Mpc. For the $s < 50\ h^{-1}$Mpc region, we plot a linear model. We see a clear sharpening of the baryonic acoustic feature after reconstruction in all cases.

All effects on the amplitude, e.g. σ_8, linear bias and linear redshift distortions, are contained in a_0 which we marginalize over.

The α parameter in equation (11) takes into account the distortion between distances measured in the fiducial cosmological model used to construct the ξ measurement, and the trial cosmological model we are testing. When applied to the baryonic acoustic feature, Eisenstein et al. (2005) argued that this distortion may be related to the cosmic distance scale as

$$\alpha = \frac{(D_{\rm V}/r_s)}{(D_{\rm V}/r_s)_{\rm fid}}, \tag{13}$$

where the volume-averaged distance is defined as

$$D_{\rm V}(z) = \left(\frac{cz(1+z)^2 D_{\rm A}^2}{H}\right)^{1/3}, \tag{14}$$

where $D_{\rm A}(z)$ is the physical angular diameter distance, $H(z)$ is the expansion rate and c is the speed of light (as defined in Hogg 1999). The calculation of the sound horizon $r_{\rm s}$ is discussed in Section 4.5. Equation (13) stems from the fact that α is the Jacobian of the volume element $\mathrm{d}^3 s$, when transforming between the true coordinate system to the fiducial one $s_{\rm f}$. Anderson et al. (2014b) showed that this is a fairly good approximation, even when there is anisotropic warping.

The template $\xi_{\rm T}$ we use is based on renormalized perturbation theory (RPT), as introduced by Crocce & Scoccimarro (2008)

$$\xi_{\rm T}(s) = \xi_{\rm L} \otimes {\rm e}^{-(k_* s)^2} + A_{\rm MC}\xi^{(1)}\frac{{\rm d}\xi_{\rm L}}{{\rm d}s}, \tag{15}$$

where the $\otimes$ term denotes convolution, L means linear, and

$$\xi^{(1)}(s) = \hat{s}\cdot\nabla^{-1}\xi_{\rm L} = \int_0^\infty \frac{k}{2\pi^2} P_{\rm L}(k) j_1(ks){\rm d}k, \tag{16}$$

where $j_1(y)$ is the spherical Bessel function of order 1.

This model has been investigated and applied by Sánchez et al. (2008, 2009, 2013), who show that it gives an unbiased measurement of α, $D_{\rm A}$, H and the equation of state of dark energy $w_{\rm DE}$.

To calculate the linear $P_{\rm L}$ and $\xi_{\rm L}$ we use the CAMB package[2] (Lewis, Challinor & Lasenby 2000) using the fiducial cosmology mentioned in Section 1. The input redshifts chosen for each redshift bin are the effective values given above.

[2] http://camb.info

Table 1. k_* values for the RPT ξ templates.

Volume	k_* pre-recon	k_* post-recon
$\Delta z^{\rm Near}$: $0.2 < z < 0.6$	0.17	0.55
$\Delta z^{\rm Mid}$: $0.4 < z < 0.8$	0.19	0.55
$\Delta z^{\rm Far}$: $0.6 < z < 1$	0.20	0.55

k_* in units of h Mpc^{-1}.

The first term in equation (15) damps the baryonic acoustic feature through the k_* parameter. The second term takes into account k-mode coupling (MC) via the $A_{\rm MC}$ parameter.

In our analysis, we fix k_* and $A_{\rm MC}$ to values corresponding to the best fits to the signal of the mock-mean correlation function ($\overline{\xi}$ hereon). These fits are performed using the covariance matrix of the mock mean, and marginalizing over the amplitude. The value of $A_{\rm MC}$ is set to 0.15, and the k_* values are summarized in Table 1.

In the pre-reconstruction case, we notice that k_* increases with redshift. This is expected because at higher redshift galaxies have less time to accumulate a displacement from their bulk flows and hence the damping scale is smaller.

The post-reconstruction fits tend to prefer a much higher k_* ($0.55\,h$ Mpc^{-1}) due to the sharpening of the peak. We test the data and the mock $\overline{\xi}$ and verify that the parameter of interest in the analysis, α, is not correlated with k_* or $A_{\rm MC}$. This verifies that our distance constraints do not depend on our choice of k_* or $A_{\rm MC}$.

The resulting templates $\xi_{\rm T}$ are displayed as the solid lines in Fig. 3, where the upper red is the pre-reconstruction template and the bottom blue is post-reconstruction. The corresponding data points are the mock $\overline{\xi}$. Although the focus of the analysis is the separation range $s = 50{-}200\,h^{-1}$Mpc, we also extrapolate in grey to the region $s < 50\ h^{-1}$Mpc, using a linear model $\xi_{\rm L}$ matched in amplitude at $50\ h^{-1}$Mpc (where RPT is no longer valid; Sánchez et al. 2008). In an analysis using a similar method Kazin et al. (2013) demonstrated that the geometric information was insensitive to the fitting range as long as the lower bound is less than $65\ h^{-1}$Mpc (see their fig. 13).

In Fig. 3, the pre-reconstruction templates show excellent agreement with the respective $\overline{\xi}$. The post-reconstruction template contains a slight downward consistent shift in ξs^2 compared to the $\overline{\xi}$, as the fit tends to be dominated by the accurate measurements at lower separations. This offset is easily accommodated by the $A(s)$ terms, and we verify below that any resulting bias in the best-fitting values of α is negligible.

3.2 Statistical methods

Throughout this analysis, we define the log-likelihood $\chi^2 \equiv -2\log L$, calculated by

$$\chi^2(\Phi) = \sum_{i,j}^{N_{\rm bins}} (m_i(\Phi) - d_i)\, C_{ij}^{-1} (m_j(\Phi) - d_j), \tag{17}$$

where m and d_i are vectors representing the models (equation 11) and data $d_i = \xi^{\Delta z}(s_i)$ (described in Section 2.4), respectively, and Φ is the parameter set which is varied.

The covariance matrix of each redshift bin used $\mathbf{C}^{\Delta z}$ is the reduced matrix '0' component of $\mathbf{C}^{\Delta z}_{[0,2]}$ given in equation (10). To correct for the bias due to the finite number of realizations used to estimate the covariance matrix and avoid underestimation of the parameter confidence limits, after inverting the matrix to $\mathbf{C}^{-1}_{\rm original}$ we multiply it by the correction factors (Hartlap, Simon & Schneider 2007; Anderson et al. 2014b)

$$\mathbf{C}^{-1} = \mathbf{C}^{-1}_{\rm original} \cdot \frac{(N_{\rm mocks} - N_{\rm bins} - 2)}{(N_{\rm mocks} - 1)}. \tag{18}$$

In our analysis, we compare separation binning of $\Delta s = 3.3$ and $6.7\,h^{-1}$Mpc. Using $N_{\rm mocks} = 600$ and $N_{\rm bins} = 23$ and 45, respectively, between [50,200] h^{-1}Mpc, we obtain correction factors of 0.96 and 0.92.

3.3 Parameter space of fitting ξ

As indicated in equation (11), the parameter space contains five parameters:

$$\Phi_{\alpha,a_i} = [\alpha, a_0, a_1, a_2, a_3]. \tag{19}$$

To sample the probability distributions of the parameter space, we use a Markov chain Monte Carlo (MCMC) based on a Metropolis–Hastings algorithm. We run the MCMC using broad priors in all of these parameters. We verify that for both the data and mocks that α is not correlated with the a_i, i.e. our distance measurements are not affected by marginalization of the shape information.

In the analysis of the chains, we report results with a prior of $|1 - \alpha| \leq 0.2$. As shown in Section 4.2, this does not have an effect on the posterior of $D_{\rm V}/r_{\rm s}$ for well-behaved realizations, i.e. realizations with well-defined baryonic acoustic feature signatures. For lower S/N realizations, i.e. for cases of a poor baryonic acoustic feature detection, this prior helps prevent the distance fits from wandering to values highly inconsistent with other measurements. Our choice of 20 per cent is well wider than the Planck Collaboration et al. (2013a) predictions of $D_{\rm V}/r_{\rm s}$ at a precision of 1.1–1.5 per cent in our redshift range of interest (this is displayed as the yellow band in Fig. 8, which is explained below).

4 RESULTS

Here, we describe results obtained in the analysis of ξ for the three redshift bins $\Delta z^{\rm Near}$ ($0.2 < z < 0.6$), $\Delta z^{\rm Mid}$ ($0.4 < z < 0.8$) and $\Delta z^{\rm Far}$ ($0.6 < z < 1$). All results are compared to those obtained when analysing the 600 WiZ-COLA mocks. Unless otherwise specified, all results described here follow the methodology described in Section 3.

4.1 Significance of detection of the baryonic acoustic feature

To quantify the sharpening of the baryonic acoustic feature in the data and mock realizations after reconstruction, we analyse the significance of its detection, as described below. Although we do not use these results for constraining cosmology, this analysis yields a first approach to understanding the potential improvement due to the reconstruction procedure.

To quantify the significance of the detection of the baryonic acoustic feature, we compare the minimum χ^2 obtained when using a physically motivated ξ template to that obtained when using a featureless template not containing baryon acoustic oscillations. For the former, we use the RPT template described in equation (15) and for the latter the 'no-wiggle' model $\xi_{\rm nw}$ presented in section 4.2 of Eisenstein & Hu (1998), which captures the broad-band shape information, excluding a baryonic acoustic feature.

The significance of the detection of the baryonic acoustic feature is determined by the square root of the difference between the

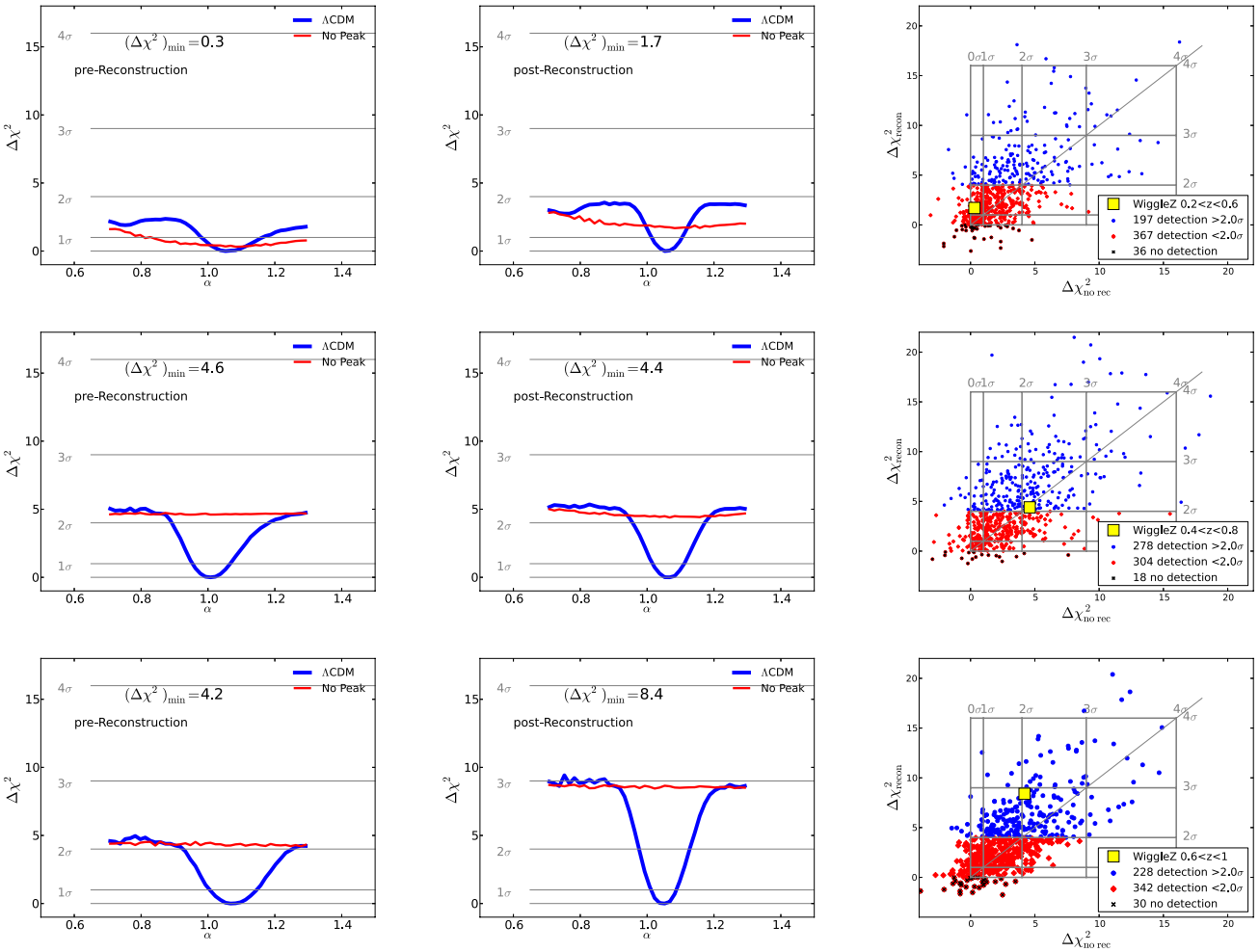

Figure 4. The minimum χ^2 as a function of α before (left) and after reconstruction (centre) for the $\Delta z^{\rm Near}$ (top), $\Delta z^{\rm Mid}$ (centre), $\Delta z^{\rm Far}$ (lower) volumes. The thick blue lines are the results when using a physical template, and the thin red line when using a no-wiggle template. The significance of detection of the baryonic acoustic feature is quantified as the square root of the difference between the minimum values of χ^2 for each template. The boundaries are the $|1-\alpha|=0.3$ prior. In all cases, there is an improvement in detection, where the most dramatic is in $\Delta z^{\rm Far}$ from 2.0σ to 2.9σ. The right-hand panels compare these data results (yellow squares) with 600 mock $\Delta\chi^2$ results pre- (x-axis) and post- (y-axis) reconstruction. The classification of detection of the significance of the baryonic acoustic feature is colour coded as indicated in the legend and explained in Section 4.1. A summary of significance of detection values for the data and mocks in all redshift bins is given in Table 2.

minimum χ^2 obtained using each template, $\Delta\chi^2$. For both calculations, we apply the same method, i.e. modelling (equation 11) and parameter space Φ_{α,a_i} (equation 19).

Fig. 4 displays the $\Delta\chi^2$ as a function of α for the WiggleZ volumes before (left-hand panels) and after reconstruction (centre panels).

Focusing first on the $\Delta z^{\rm Far}$ volume, we see a significant improvement in the detectability of the baryonic acoustic feature after applying reconstruction. The result obtained before reconstruction shows a low significance of detection of $\sqrt{4.2}=2\sigma$ compared to that obtained after reconstruction $\sqrt{8.4}=2.9\sigma$.

These results are for a binning of $\Delta s=3.3\,h^{-1}$Mpc. When using $\Delta s=6.7\,h^{-1}$Mpc, both $\Delta\chi^2$ are lower (2.3 and 7.2, respectively), but the difference between the pre- and post-reconstruction values remains similar $\Delta(\Delta\chi^2)\sim 4.5$.

The right-hand panels of Fig. 4 show a comparison of these WiggleZ results (yellow square) to that expected from an array of 600 WiZ-COLA mocks. To facilitate interpretation of the results, we indicate realizations which contain at least a 2σ detection in the post-reconstruction case, which is characteristic of the data. The realizations in which we detect a feature better than this threshold are displayed in blue circles ($\Delta z^{\rm Near}$: 197/600 mocks, $\Delta z^{\rm Mid}$: 278/600, $\Delta z^{\rm Far}$: 228/600) compared to those in which we do not in red diamonds ($\Delta z^{\rm Near}$: 367/600 mocks, $\Delta z^{\rm Mid}$: 304/600, $\Delta z^{\rm Far}$: 342/600). The crosses are a subset for which the $\Delta\chi^2$ is negative, meaning the no-wiggle template fit is better than that of the physical template ($\Delta z^{\rm Near}$: 36/600 mocks, $\Delta z^{\rm Mid}$: 18/304, $\Delta z^{\rm Far}$: 30/600).

From these mock results, we learn about a few aspects of the results in the $\Delta z^{\rm Far}$ volume. First, the average mock realization yields a fairly low significance of detection, where both pre- and post-reconstruction are between 1and2σ, and in 5 per-cent of the mocks the physical $\xi_{\rm T}$ completely fails to outperform $\xi_{\rm nw}$.

Secondly, we see that after applying reconstruction, there is a moderate improvement in the detectability of the baryonic acoustic feature. This can be quantified by a change in the median detectability of 1.4σ–1.7σ, both with an rms of 0.8σ (the negative $\Delta\chi^2$ values are set to zero in this calculation). When focusing on the $>2\sigma$ detection subsample (where the threshold is applied to

Table 2. Significance of detection of the baryonic acoustic feature.

Volume	$\sqrt{\Delta\chi^2}$	$\chi^2_{\rm phys}$, $\chi^2_{\rm nw}$	Expected (All mocks)	Expected ($>2\sigma$ subsample)
$\Delta z^{\rm Near}$ no recon	0.5	18.0, 18.3	1.4±0.8 (600)	2.0±0.8 (197)
$\Delta z^{\rm Near}$ w/ recon	1.3	24.3, 26.0	1.6±0.9 (600)	2.4±0.5 (197)
$\Delta z^{\rm Mid}$ no recon	2.1	20.5, 25.1	1.7±0.9 (600)	2.1±0.8 (278)
$\Delta z^{\rm Mid}$ w/ recon	2.1	9.1, 13.5	1.9±0.9 (600)	2.6±0.6 (278)
$\Delta z^{\rm Far}$ no recon	2.0	24.3, 28.5	1.5±0.8 (600)	2.0±0.7 (228)
$\Delta z^{\rm Far}$ w/ recon	2.9	24.0, 32.4	1.7±0.8 (600)	2.5±0.5 (228)

All columns, except the second to the left ($\chi^2_{\rm phys}$, $\chi^2_{\rm nw}$), are in terms of σ detection.

The significance of detection in each volume is determined by $\sqrt{\Delta\chi^2}$, where $\Delta\chi^2 \equiv \chi^2_{\rm nw} - \chi^2_{\rm phys}$ and dof = 18.

$\Delta z^{\rm Near}$: $0.2 < z < 0.6$, $\Delta z^{\rm Mid}$: $0.4 < z < 0.8$, $\Delta z^{\rm Far}$: $0.6 < z < 1$

The $>2\sigma$ subsample is based on results of the post-reconstruction case.

the post-reconstruction results), the improvement is slightly better, from a median of 2.0σ (rms of 0.7σ) to a median 2.6σ with an rms of 0.5σ. In Section 4.2, we find, that, on average, this translates into an improvement in accuracy of the $D_{\rm V}/r_{\rm s}$ measurement.

Thirdly, whereas the pre-reconstruction detection significance in the data appears similar to an average realization, the post-reconstruction detection is on the fortunate side (top 8 percentile of all 600 mocks). We show the corresponding improvement in the measurement of $D_{\rm V}/r_{\rm s}$ in Section 4.2. These data and mock results, as well as those for $\Delta z^{\rm Near}$ and $\Delta z^{\rm Mid}$, are summarized in Table 2.

We turn now to examine the other two redshift bins. In the top panels of Fig. 4 and in Table 2, we see that the detection in the WiggleZ $\Delta z^{\rm Near}$ volume improves from no clear preference of $\xi_{\rm T}$ over $\xi_{\rm nw}$ before reconstruction, to a weak detection of 1.3σ after. In the pre-reconstruction case, this volume appears to be underperforming compared to the mock results. In the post-reconstruction case, its performance appears to be within expectations of the mocks.

According to the mock catalogues, the performance of the $\Delta z^{\rm Mid}$ volume should be the best amongst the three Δz volumes. This is evidenced by the fact that the $>2\sigma$ subset is larger (278/600) than the others (197 and 224). This reflects the fact that this redshift range contains the highest effective volume, i.e. the best combination of shot-noise and sample variance of the three. The effective volume numbers are evaluated at $k = 0.1\,h/$ Mpc in units of h^{-3} Gpc^3: 0.096 ($\Delta z^{\rm Near}$), 0.130 ($\Delta z^{\rm Mid}$), 0.089 ($\Delta z^{\rm Far}$). This does not, however, translate into notable improvements in the average significance of detection or constraints on $D_{\rm V}/r_{\rm s}$ in the mocks or in the data. In the data, as we shall continue to see, the redshift bin that benefits the most from the reconstruction procedure is $\Delta z^{\rm Far}$. The mock results suggest that this is due to sample variance reasons.

From Table 2, we also learn that reconstruction improves the significance of detection of the baryonic acoustic feature for the average mock by $\sim 0.2-0.3\sigma$, whereas the $>2\sigma$ subsample improves by $0.4-0.5\sigma$. We also note that the scatter of the significance of detection in the generic case does not vary, but in the $>2\sigma$ subsample improves from $0.7-0.8\sigma$ pre-reconstruction to $0.5-0.6\sigma$ post-reconstruction.

Blake et al. (2011) reported pre-reconstruction significance of detections 1.9σ, 2.2σ, 2.4σ, which are slightly higher than those reported here. Their results are expected to yield a higher detection significance through using a fixed shape of ξ, whereas we vary the shape in the fit (as described in Section 3). This could be understood, e.g. by the fact that the full shape of ξ analysis assumes a cosmology, and hence explores a smaller parameter space, leading to a higher significance of detection. In our analysis, we make no assumption of a prior cosmology, effectively marginalizing over a much larger parameter space, and hence, we report a more model-independent significance of detection.

To summarize, we find that reconstruction improves the detectability of the baryonic acoustic feature in the majority of the WiZ-COLA volumes. For the $\Delta z^{\rm Near}$ volume, we find improvement of detectability for 373/600 of the mocks, in $\Delta z^{\rm Near}$ for 389/600 and in $\Delta z^{\rm Far}$ for 378/600. Hence, we learn that there is an $\sim$65 per cent probability of improvement of detection of the baryonic acoustic feature in WiggleZ volume due to reconstruction. In the case of the data, we find moderate improvement for $\Delta z^{\rm Near}$, no improvement for $\Delta z^{\rm Mid}$ and significant improvement for $\Delta z^{\rm Far}$.

4.2 Distance constraints

We now turn to using the baryonic acoustic feature to constrain $D_{\rm V}/r_{\rm s}$. We quote the final results in terms of $D_{\rm V}(r_{\rm s}^{\rm fid}/r_{\rm s})$ in order not to assume the sound horizon obtained with the fiducial cosmology $r_{\rm s}^{\rm fid}$. This is further discussed in Section 4.3. Fig. 5 displays the posterior probability distributions of $D_{\rm V}(r_{\rm s}^{\rm fid}/r_{\rm s})$ for all three WiggleZ Δz bins, both pre- (dashed red) and post-reconstruction (solid blue). The dotted magenta lines are Gaussian distributions based on the mode values and the half-width of the 68 per cent confidence region of the post-reconstruction case (not the best-fitting Gaussian to the posterior). A summary of the statistics may be found in Table 3, as well as in the panels of Fig. 5.

We find that in all three redshift bins, the $D_{\rm V}(r_{\rm s}^{\rm fid}/r_{\rm s})$ constraints improve with the application of reconstruction. As noted above, the most dramatic improvement is for $\Delta z^{\rm Far}$ ($0.6 < z < 1$) which is shown in the right-hand panel of Fig. 5 (as well as the left and centre of the bottom panels of Fig. 4). As indicated in Table 3 the width of the 68 per cent confidence region improves from 7.2 to 3.4 per cent accuracy. This improvement can be attributed to the clear sharpening of the baryonic acoustic feature as seen in Fig. 2, which makes the peak-finding algorithm much more efficient. Here, we fix the damping parameter k_* and $A_{\rm MC}$. When relaxing this assumption we obtain similar results. Here, we use a binning of $\Delta s = 6.7\,h^{-1}$Mpc, but find consistent results for $\Delta s = 3.3\,h^{-1}$Mpc.

The clear cut-off that is seen in some of the posteriors (mostly the pre-reconstruction) is due to the $|1-\alpha| < 0.2$ flat prior described in Section 3.3. This prior does not appear to have an effect on the post-reconstructed posteriors. We attribute the elongated wings of the posteriors seen in some cases to the low significance of detection of the baryonic acoustic feature in the pre-reconstruction cases for $\Delta z^{\rm Near}$ and $\Delta z^{\rm Far}$.

We find that the maximum likelihood values of $D_{\rm V}(r_{\rm s}^{\rm fid}/r_{\rm s})$ at all redshifts are consistent before and after reconstruction, within

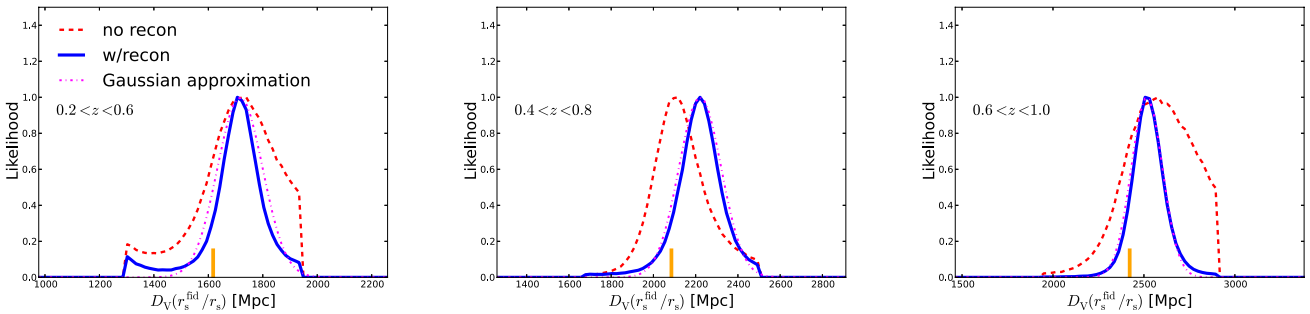

Figure 5. The $D_V(r_s^{fid}/r_s)$ posterior probability distributions of the three WiggleZ Δz volumes (as indicated), for both pre- (dashed red) and post-reconstruction (solid blue). Gaussian approximations based on the mode and standard deviation values of the post-reconstruction cases are shown in dot–dashed magenta. In each panel, we quote $D_V(r_s^{fid}/r_s)$ and its 68 per cent confidence region, the $\alpha \equiv (D_V/r_s)/(D_V/r_s)_{fid}$ value, and plot the orange vertical line at the fiducial value $\alpha = 1$ for comparison. The sharp cut-off in some of the results is due to the $|1 - \alpha| < 0.2$ prior. The improvement due to reconstruction is apparent in all Δz bins. These results are summarized in Table 3.

Table 3. Distance measurement summary.

Effective z	Data α (%)	Data $D_V(r_s^{fid}/r_s)$ [Mpc]	Mock α results	Mock σ_α results (# mocks)
0.44 no recon	1.065 (7.9%)	1723^{+122}_{-151}	1.005±0.067	0.051±0.027 (197)
0.44 w/ recon	1.061 (4.8%)	$\mathbf{1716^{+73}_{-93}}$	1.005±0.048	0.034±0.010 (197)
0.60 no recon	1.001 (6.0%)	2087^{+156}_{-95}	1.002±0.051	0.049±0.023 (278)
0.60 w/ recon	1.065 (4.5%)	$\mathbf{2221^{+97}_{-104}}$	1.003±0.037	0.032±0.010 (278)
0.73 no recon	1.057 (7.2%)	2560^{+215}_{-157}	1.0004±0.059	0.050±0.022 (228)
0.73 w/ recon	1.039 (3.4%)	$\mathbf{2516^{+94}_{-78}}$	1.003±0.050	0.037±0.013 (228)

The columns marked by 'data' are the WiggleZ results, and those by 'mock' are simulated.
The effective z are for volumes Δz^{Near}: $0.2 < z < 0.6$, Δz^{Mid}: $0.4 < z < 0.8$, Δz^{Far}: $0.6 < z < 1$
$\alpha \equiv (D_V/r_s)/(D_V/r_s)_{fid}$.
The figures in brackets in the 'data α' column is the half-width of the 68 per cent confidence region.
To convert α to $D_V(r_s^{fid}/r_s)$, we use fiducial values of D_V^{fid} for the three Δz (in Mpc): 1617.7, 2085.2, 2421.7, respectively.
The $^+_-$ values for the $D_V(r_s^{fid}/r_s)$ column are the 68 per cent confidence region, as calculated from the edges inwards.
The cross-correlation of the $D_V(r_s^{fid}/r_s)$ results is indicated in Table 4.
The mock median and std results for α and σ_α are from the $>2\sigma$ detection subsamples, as indicated. These are not Gaussian.

the 68 per cent confidence regions, and see a clear overlap of the posteriors. This is in agreement with predictions from mock catalogues, which indicate that we would expect a cross-correlation of 0.55−0.65 between the $D_V(r_s^{fid}/r_s)$ measurements before and after reconstruction (see the top panels of Fig. 6, which is described below).

To better understand expectations of results in the three WiggleZ volumes, we apply our analysis pipeline to 600 WiZ-COLA mocks in each Δz volume. Results are displayed in Fig. 6. Each column represents results of a different Δz bin, as indicated. In the top row are the α distributions pre- and post-reconstruction, and the panels in the bottom row are the distribution of the uncertainty in the fit to each realization σ_α. Similar to the right-hand panel of Fig. 4, the colour coding is such that realizations with a detection of the baryonic acoustic feature above the threshold of 2σ in the reconstruction case are in blue circles, below are in red diamonds, and no detection are marked by X. Also displayed are dashed lines which indicate the median values of the $>2\sigma$ subset, as well as the cross-correlation values r of this subset. In the bottom row, we also indicate the WiggleZ σ_α results for comparison in the yellow boxes. In Table 3, we summarize statistics for these distributions for the $>2\sigma$ subset, which can be compared to the data.

In the top row of Fig. 6, we notice in all Δz bins groupings along the boundaries of boxes with sides at $|1 - \alpha| = 0.2$ from the centre, the hard prior we set in the analysis. These indicate failures of determining α in these realizations, which is dominantly from the $<2\sigma$ subsets, i.e. when the S/N ratio is low.

Compared to the fiducial cosmology of the mocks $\alpha = 1$ the distribution of fitted α yields a median bias between 0.04 and 0.5 per cent, which is much smaller than the statistical uncertainties. We also test the peak finding algorithm on the mock $\bar{\xi}$ and find fairly good agreement with the median α results of the $>2\sigma$ subsample reported in Table 3.

The reconstruction cases demonstrate a clear improvement in the scatter of α, as seen in Table 3. For the $>2\sigma$ subset, the scatter is reduced from 5–6.5 per cent to 3.5–5 per cent. A similar improvement in the scatter is obtained when examining the full sample.

In the bottom row of Fig. 6, we see that reconstruction results in moderate to dramatic improvements in most of the σ_α results. The 2σ threshold of detection of the baryonic acoustic feature also shows clear trends that the $<2\sigma$ subsample (red diamonds) does not constrain α as well as the $>2\sigma$ subsample (blue circles). This dramatic improvement is also shown in the right-hand column in Table 3, where the median σ_α improves in all z bins from 5 per cent with a scatter of ∼2.2–2.7 per cent to 3.2–3.7 per cent

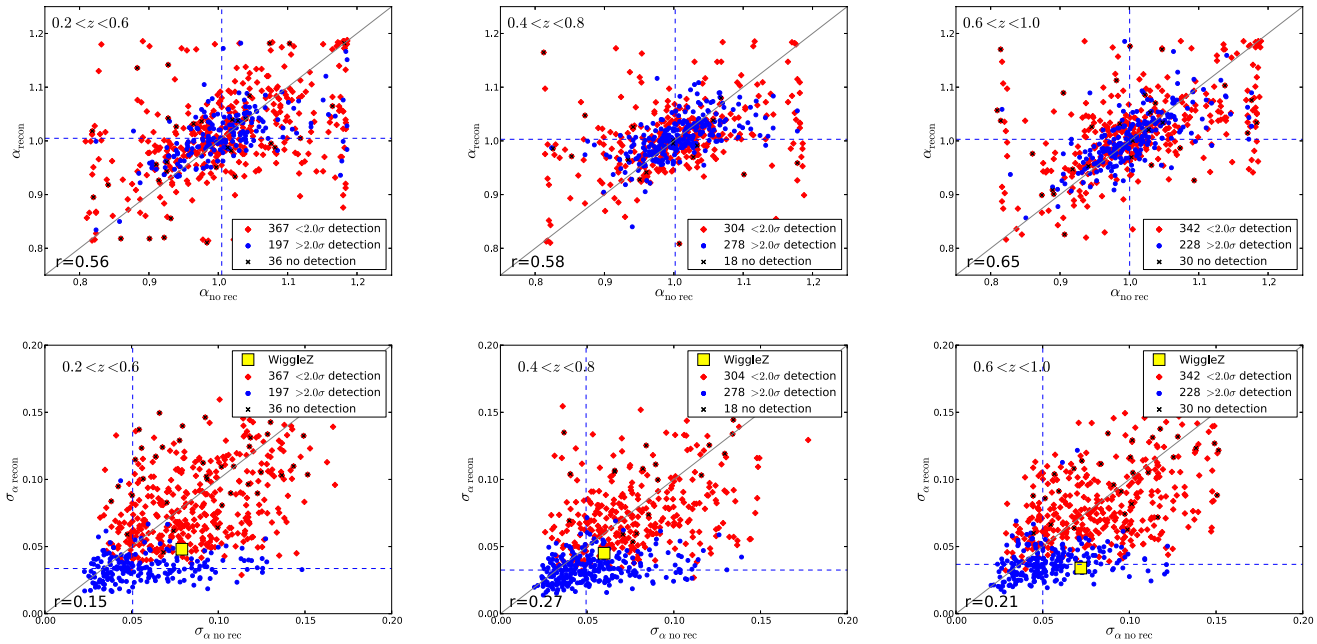

Figure 6. The top row shows the distribution of best-fitting α for the 600 mocks for the three redshift bins as indicated before (x-axis) and after (y-axis) reconstruction. The bottom row is the same for the uncertainties σ_α of the mocks, as well as the WiggleZ data (yellow squares). The blue circles are results of realizations in which the significance of detection of the baryonic acoustic feature after reconstruction is better than 2σ, and the red diamonds are for mocks below this threshold. The marked Xs are realizations in which the $\xi_{\rm nw}$ template outperforms the physical one. The dashed lines indicate the median of each statistic for the $>2\sigma$ detection subsamples, and r is the correlation coefficient of this subsample. There is a clear trend of the $>2\sigma$ detection realizations yielding tighter σ_α constraints. WiggleZ results and summaries of the mocks are in Table 3.

with a scatter of 1 per cent. Examining the full 600 mocks in each Δz, there is a similar improvement in the median, but not in the scatter.

Distributions of α and σ_α across the mocks show significant non-Gaussian tails. We attribute this to the effect of low-significance detection of the baryonic acoustic feature. We perform Kolmogorov–Smirnov tests for Gaussianity of α and σ_α and find the p-values to be negligible. In the regime where the baryonic acoustic feature is being just resolved, there is a steep non-linear relation between the significance of detection of the baryonic acoustic feature and the uncertainty in α, which is demonstrated in Fig. 7. Here, we display the significance of detection of the baryonic acoustic feature and the resulting σ_α of all realizations for the post-reconstruction case in all three Δz volumes. We see a transition from a somewhat linear relationship for the $>2.5\sigma$ significance of detection realizations to a more non-linear relationship below this threshold.

The values of the uncertainties of $D_{\rm V}(r_{\rm s}^{\rm fid}/r_{\rm s})$ obtained for the WiggleZ data in each redshift slices lie within the range covered by the mocks in both pre- and post-reconstruction cases.

We next briefly discuss cosmological implications of these improved measurements.

4.3 Distance–redshift relation summary

Fig. 8 summarizes the model-independent $D_{\rm V}/r_{\rm s}$ results obtained here pre- (red; left-hand panel) and post-reconstruction (blue; both panels). All results are divided by the distance–redshift relation for the fiducial cosmology used for analysis. These new WiggleZ measurements (blue and red) are also indicated in Table 3.

Also plotted in the left-hand panel of Fig. 8 are the WiggleZ $d_z \equiv r_{\rm s}/D_{\rm V}$ results from the Blake et al. (2011) analysis: $(0.0916 \pm 0.0071, 0.0726 \pm 0.0034, 0.0592 \pm 0.0032)$ for $z_{\rm eff} = 0.44, 0.6, 0.73$, respectively. There are a few differences in methodology between our pre-reconstruction analysis and theirs. The most important difference is that they focus on the information in the full shape of ξ, where we marginalize over shape and focus only on the peak position, making our results model independent. However, despite these differences, the results of the two analyses are consistent.

For comparison in the right-hand panel of Fig. 8, we plot $D_{\rm V}/r_{\rm s}$ measurements by Padmanabhan et al. (2012, 8.88 ± 0.17; $z = 0.35$), Anderson et al. (2014a, $D_{\rm V}(r_{\rm s}^{\rm fid}/r_{\rm s}) = 1264 \pm 25$ Mpc, 2056 ± 20 Mpc at $z = 0.32, 0.57$, respectively) and $d_z(z = 0.106) = 0.336 \pm 0.015$ from Beutler et al. (2011). As pointed out by Mehta et al. (2012), there are discrepancies in the literature regarding the calculation of $r_{\rm s}$. A common approximation is using equations 4– 6 in Eisenstein & Hu (1998). A more generic treatment is obtained by using the full Boltzmann equations as used in the CAMB package (Lewis et al. 2000, e.g. this takes into account the effect of neutrinos). Calculations show that these differ by over 2 per cent, which is now worse than the current 0.4 per cent accuracy measurements of Planck Collaboration et al. (2013a). Although Mehta et al. (2012) show that differences in methods do not yield significant variations of $r_{\rm s}/r_{\rm s}^{\rm fid}$ when varying a cosmology from a fiducial, direct comparisons of results require a uniform method. For this reason, because our choice of preference is using CAMB, we re-scale the $D_{\rm V}/r_{\rm s}$ results of Padmanabhan et al. (2012) and Beutler et al. (2011) by $r_{\rm s\ EH98}^{\rm fid-study}/r_{\rm s\ CAMB}^{\rm fid-study}$, according to the fiducial cosmologies reported in the each study, fid-study (1.025 and 1.027, respectively). For the Anderson et al. (2014a) results, we use their calculation of $r_{\rm s\ CAMB}^{\rm fid-study} = 149.28$ Mpc.

In Fig. 8, we also plot predictions for models based on flat ΛCDM, according to best-fitting parameters obtained by Komatsu et al. (2009, dot–dashed line; this is our fiducial cosmology), Sánchez et al. (2013, short dashed line) and Planck

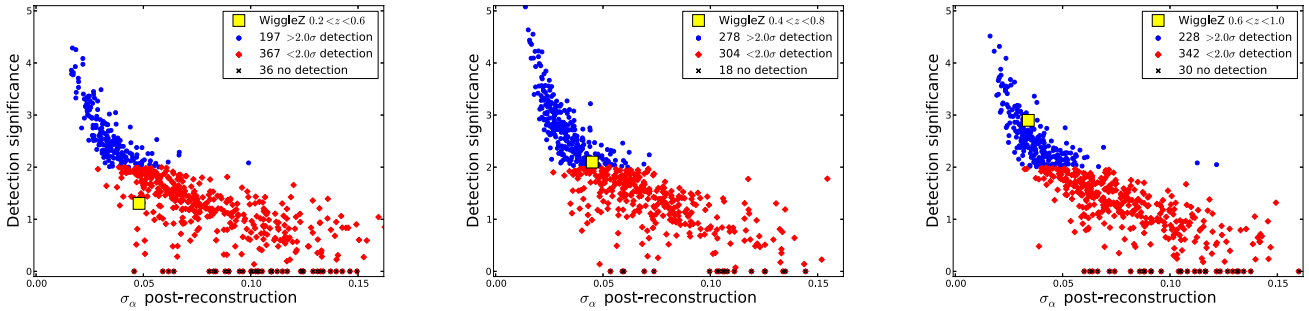

Figure 7. For each volume, we plot the post-reconstruction significance of detection of the baryonic acoustic feature against the resulting σ_α for each mock realization. As in previous figures, the colour coding is such that blue circles are realizations in the $>2\sigma$ subsample, red diamonds are from the $<2\sigma$ subsample, and Xs do not yield a detection. The WiggleZ data points are indicated by the yellow squares.

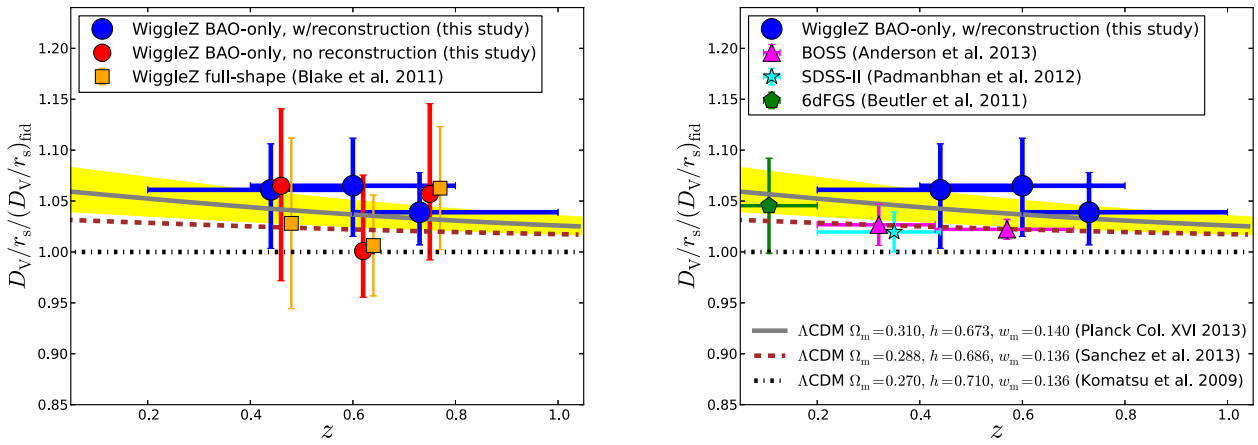

Figure 8. Both panels display the volume-averaged distance to sound-horizon ratios D_V/r_s normalized by the fiducial value, where the post-reconstruction results are indicated by the large blue circles. In the left-hand panel, the no reconstruction BAO-only results (red circles) and the ξ shape analysis results (Blake et al. 2011, orange squares) are slightly shifted for clarity. In the right-hand panel, we compare with two results from the SDSS-II (cyan star, $0.2 < z < 0.44$; Padmanabhan et al. 2012) and SDSS-III (magenta triangles $0.2 < z < 0.43$ $0.43 < z < 0.7$; Anderson et al. 2014a), as well as the result obtained by the 6dFGS ($z \sim 0.1$; Beutler et al. 2011). In both panels, the cosmology prediction lines are best-fitting flat ΛCDM results (ΛCDM) obtained by Planck (Planck Collaboration et al. 2013a; solid) where the yellow band is the 68 per cent confidence region, SDSS-BOSS (Sánchez et al. 2013; dashed), *WMAP* (Komatsu et al. 2009; dot–dashed). The y-axis uncertainty bars are the 68 per cent confidence region, and those on the x-axis indicate the redshift range of analysis.

Collaboration et al. (2013a, solid line), where the wide yellow band shows the 68 per cent confidence region using COSMOMC. The Ω_m, h and $w_m \equiv \Omega_m h^2$ of each model are indicated in the legend.

Of the three predictions, our results appear to agree best with those reported by Planck Collaboration et al. (2013a, solid line), which obtain $h \sim 0.67$, where the local expansion rate is defined by $H_0 \equiv 100\,h(\mathrm{km})(\mathrm{Mpc})^{-1}(\mathrm{s})^{-1}$. When analysing various data sets below in Section 4.5 we show that our h results are similar to those of Planck Collaboration et al. (2013a) rather than the lower value obtained by *Wilkinson Microwave Anisotropy Probe* (*WMAP*; dot–dashed) of $h \sim 0.71$.

4.4 Covariance matrix of D_V/r_s

Before presenting cosmological implications, we first discuss the calculation of the covariance between measurements in different redshift slices. Due to the overlap between Δz^{Mid} ($0.4 < z < 0.8$) and the other redshift bins, we calculate the correlation coefficients between the α results obtained using the 300 *stitched* Δz^{Mid} mock catalogues (see Section 2.2) and the corresponding Δz^{Near} and Δz^{Far} catalogues. We apply the same α fitting algorithm as before and present comparisons of the results in Fig. 9. The top two panels are before reconstruction and the bottom panels are after reconstruction. For all panels, the x-axis values are the α results when using the stitched Δz^{Mid} volume, and the y-axis values are for the corresponding Δz^{Near} (left-hand column) and Δz^{Far} (right) volumes. As before, we colour-code the results according to the significance of detection of the baryonic acoustic feature, where the reference subsample for this classification is the stitched Δz^{Mid} case.

Focusing on the $>2\sigma$ subsample in each case, we find that the correlation coefficient between the stitched Δz^{Mid} and its overlapping neighbours is $r \sim 0.35-0.45$. We verify that between Δz^{Near} and Δz^{Far} $r \sim 0$. We use these and the uncertainties in Table 3 to construct the covariance matrix of the WiggleZ post-reconstruction D_V/r_s. The inverse covariance matrix is presented in Table 4.

4.5 Cosmological implications

We next examine cosmological implications of the new distance–redshift measurements. In this analysis, we use the reconstructed WiggleZ $D_V(r_s^{\mathrm{fid}}/r_s)$ results listed in Table 3, and their inverse covariance matrix (Table 4).

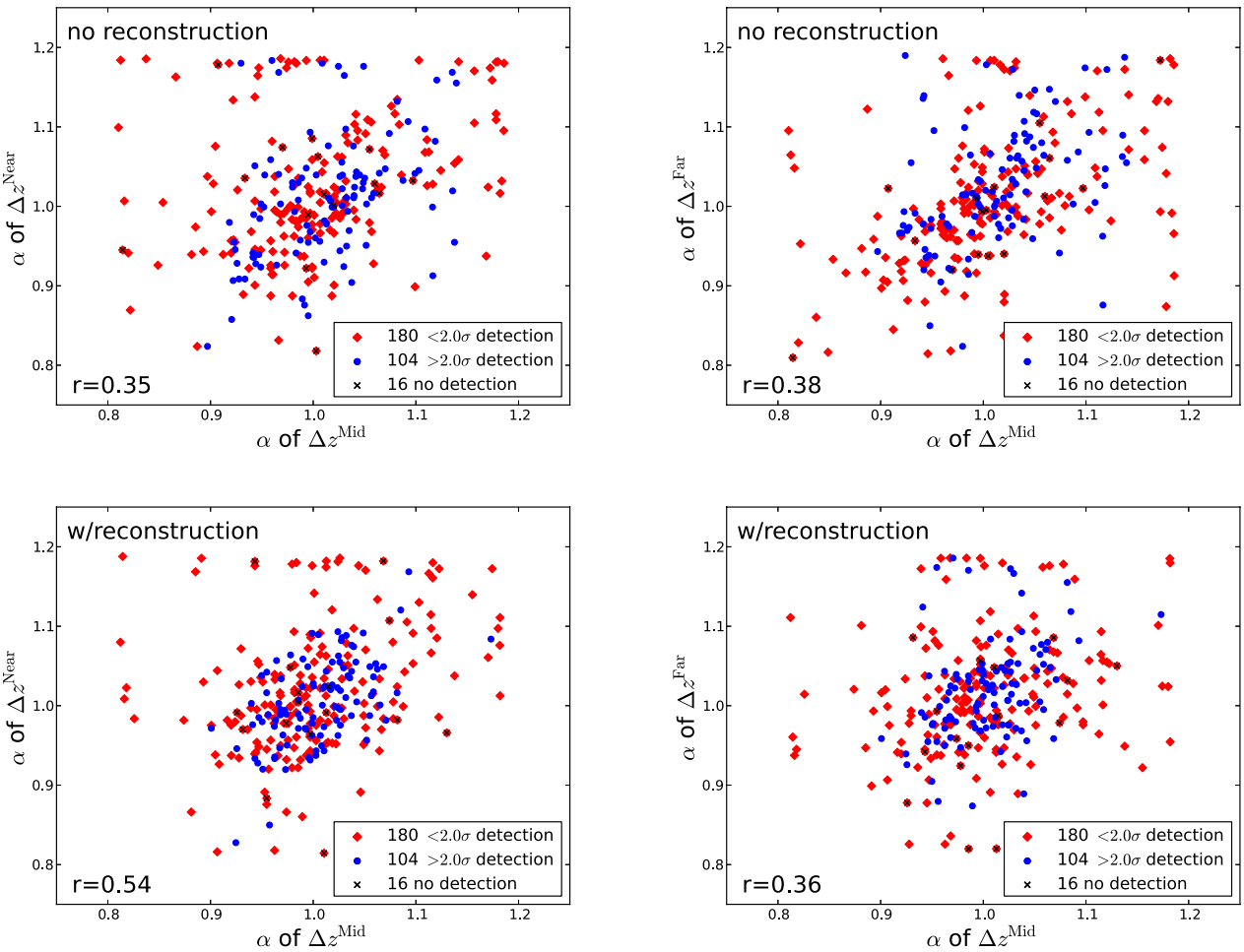

Figure 9. The top row shows the α distribution of the 300 mocks for the no reconstruction case and the bottom for post-reconstruction. In each, the x-axes values are those obtained with the $\Delta z^{\rm Mid}$ ($0.4 < z < 0.8$) realizations, and the y-axes values are for $\Delta z^{\rm Near}$ ($0.2 < z < 0.6$; left-hand panels) and $\Delta z^{\rm Far}$ ($0.6 < z < 1$; right-hand panels), accordingly. The blue circles are results of realizations in which the significance of detection of the baryonic acoustic feature after reconstruction is better than 2σ, and the red diamonds are for mocks below this threshold, Xs indicate realizations with no detection. The correlation coefficient r for the $>2\sigma$ subsample is indicated in the bottom left of each panel.

Our base model corresponds to an energy budget consisting of baryons (b), radiation (r), CDM and the so-called dark energy. The primordial density fluctuations are adiabatic and Gaussian with a power-law spectrum of Fourier amplitudes.

Table 4. The inverse covariance matrix of the $D_{\rm V}(r_{\rm s}^{\rm fid}/r_{\rm s})$ measurements from the reconstructed WiggleZ survey data. The volume-averaged distance is defined in equation (14) and $r_{\rm s}$ is the sound horizon at $z_{\rm drag}$, and the fiducial cosmology assumed is given in Section 1. These measurements are performed in three overlapping redshift slices $0.2 < z < 0.6$, $0.4 < z < 0.8$, $0.6 < z < 1$ with effective redshifts of 0.44, 0.6, 0.73 respectively. The data vector is $D_{\rm V}(r_{\rm s}^{\rm fid}/r_{\rm s})$ =[1716.4, 2220.8, 2516.1] Mpc as listed in Table 3. As the matrix is symmetric we quote the upper diagonal, and for brevity multiply by a factor of 10^4 Mpc^2. That is, the user should multiply each element by this factor, e.g. the first element would be 2.17898878 10^{-4} Mpc^{-2}.

Redshift slice	$0.2 < z < 0.6$	$0.4 < z < 0.8$	$0.6 < z < 1$
$0.2 < z < 0.6$	2.178 988 78	−1.116 333 21	0.469 828 51
$0.4 < z < 0.8$		1.707 120 04	−0.718 471 55
$0.6 < z < 1.0$			1.652 831 75

We investigate four models. The first is the flat cosmological constant CDM paradigm, where the equation of state of dark energy is set to $w = -1$ (ΛCDM). We then relax the assumption of flatness ($o\Lambda$CDM). We also investigate the variation of w both when assuming flatness (wCDM), as well as without (owCDM)

The main advantage of using information from low-redshift surveys $z < 1$ is their ability to constrain the equation of state of dark energy w and the curvature $\Omega_{\rm K}$, which are otherwise degenerate when analysing the CMB on its own. This is understood through the relationship between the expansion rate $H(z)$ and the cosmic composition:

$$H(z)^2 = H_0^2\Big(\Omega_{\rm M}(1+z)^3 + \Omega_{\rm K}(1+z)^2 + \Omega_r(1+z)^4 + \Omega_{\rm DE}e^{3\int_0^z \frac{1+w(z')}{1+z'}{\rm d}z'}\Big), \quad (20)$$

where $\sum_i \Omega_i = 1$ for $i =$ m, K, r, DE. According to the definition of $D_{\rm V}$ (equation 14), our $D_{\rm V}(r_{\rm s}^{\rm fid}/r_{\rm s})$ measurements yield degeneracies between H, $D_{\rm A}$ and the sound horizon at the end of the drag epoch $r_{\rm s}$.

The physical angular diameter distance[3]

$$D_{\rm A} = \frac{1}{1+z}\frac{c}{H_0}\frac{1}{\sqrt{-\Omega_{\rm K}}}\sin\left(\sqrt{-\Omega_{\rm K}}\frac{\chi}{c/H_0}\right) \quad (21)$$

integrates over H through the definition of the comoving distance:

$$\chi(z) = c\int_0^z \frac{{\rm d}z'}{H(z')}. \quad (22)$$

We calculate the sound horizon $r_{\rm s}$ and the end-of-drag redshift $z_{\rm d}$ by using CAMB (Lewis et al. 2000). For our fiducial cosmology we obtain $r_{\rm s}^{\rm fid}$ =148.6 Mpc. We point out that another popular choice of calculating $r_{\rm s}$ is by using equation 6 of Komatsu et al. (2009) and $z_{\rm d}$ with their equations 3– 5. With this we obtain $r_{\rm s}^{\rm fid}$ =152.3 Mpc. We do not use this last calculation in our analysis. See Section 4.3 for a discussion regarding these differences across other survey results.

Information from the CMB is required to break the degeneracy with the sound horizon scale $r_{\rm s}$. For this purpose, we use the *Planck* CMB temperature anisotropies (Planck Collaboration et al. 2013b), and the CMB polarization measurements from *WMAP*9 (Bennett et al. 2013). When analysing the CMB information we vary the physical baryon density $w_{\rm b} \equiv \Omega_{\rm b}h^2$, the physical CDM density $w_{\rm c} \equiv \Omega_{\rm c}h^2$, the ratio of the sound horizon to the angular diameter distance at the last-scattering surface Θ, the Thomson scattering optical depth due to reionization τ, the scalar power-law spectral index $n_{\rm s}$ and the log power of the primordial curvature perturbation $\ln(10^{10}A_{\rm s})$ (at $k = 0.05$ Mpc^{-1}).

The CMB anisotropies also depend on the following parameters, which we fix: the sum of neutrino masses $\sum m_\nu$ =0.06eV, the effective number of neutrino-like relativistic degrees of freedom $N_{\rm eff}$ = 3.046, the fraction of baryonic mass in helium $Y_{\rm P} = 0.24$, the amplitude of the lensing power relative to the fiducial value $A_{\rm L} = 1$. We also set to zero the effective mass of sterile neutrinos $m^{\rm eff}_{\nu,\ {\rm sterile}}$, the tensor spectrum power-law index $n_{\rm t}$, the running of the spectral index ${\rm d}n_{\rm s}/{\rm d}\ln k$ and the ratio of tensor primordial power to curvature power $r_{0.05}$. Planck Collaboration et al. (2013a) describe the nuisance parameters that are marginalized when fitting the CMB data.

In addition, we use the 6dF Galaxy Survey (6dFGS) BAO measurement $r_{\rm s}/D_{\rm V} = 0.336 \pm 0.015$ obtained by Beutler et al. (2011). Lastly, to quantify the improvements due to using the reconstructed WiggleZ $D_{\rm V}(r_{\rm s}^{\rm fid}/r_{\rm s})$, we compare all results to those obtained when using the $A(z) \propto D_{\rm V}\sqrt{w_{\rm M}}$ measurements of Blake et al. (2011). They conclude that, when using the full shape of ξ as a standard ruler, the $A(z)$ parameter, as introduced by Eisenstein et al. (2005), is a more appropriate representation of the BAO information. The values used here at $z = 0.44, 0.6, 0.73$ are listed in their table 5, and their inverse covariance matrix in their table 2.

We use the COSMOMC package (October 2013 version; Lewis et al. 2002) to calculate the posteriors. The algorithm explores cosmological parameter space by Monte Carlo sampling data sets where it does accurate calculations of theoretical matter power spectrum and temperature anisotropy C_ℓ calculations using CAMB (Lewis et al. 2000).

In our MCMC runs, we test the following combinations of data:

(i) CMB: *Planck* temperature fluctuations (Planck Collaboration et al. 2013b) and *WMAP*9 polarization (Bennett et al. 2013).

(ii) CMB+(WiggleZ pre-recon): CMB with the $A(z)$ pre-reconstruction constraints from Blake et al. (2011).

(iii) CMB+(WiggleZ post-recon): CMB with post-reconstruction $D_{\rm V}(r_{\rm s}^{\rm fid}/r_{\rm s})$ results investigated here.

(iv) CMB+(WiggleZ post-recon)+6dFGS: same as CMB+(WiggleZ post-recon) with the addition of the baryonic acoustic feature results from the 6dFGS.

For comparison, we also test CMB with the 6dFGS results without information from WiggleZ.

Here, we report results for the local expansion rate H_0, the density of matter $\Omega_{\rm m}$, the equation of state of dark energy w and the curvature parameter $\Omega_{\rm K}$, as relevant in the tested models.

Our results are summarized in Table 5 and in Fig. 10. All the results show consistency with the flat ($\Omega_{\rm K} = 0$) cosmological constant ($w = -1$) CDM paradigm. In the following subsections, we describe the main results of the four models tested.

4.5.1 Λ*CDM results*

The top-left panel of Fig. 10 presents the joint posterior probability distribution of H_0 and $\Omega_{\rm m}$, and the marginalized results are summarized in Table 5. These measurements follow the degeneracy line of constant $\Omega_{\rm m}h^3$ (e.g. Percival et al. 2002; Sanchez et al. 2014). All combinations of data sets tested yield consistent results. There is a moderate improvement when adding the reconstructed WiggleZ $D_{\rm V}(r_{\rm s}^{\rm fid}/r_{\rm s})$ information to that of the CMB. This can be quantified by the marginalized measurement of H_0 improving from 1.8 to 1.5 per cent accuracy, and $\Omega_{\rm m}$ from 5.4 to 4.7 per cent accuracy. Comparing CMB+(WiggleZ no recon) to the other combinations, we conclude that the reconstruction of WiggleZ and the additional information from 6dFGS does little to improve the H_0 and $\Omega_{\rm m}$ measurements.

4.5.2 *wCDM results*

We now allow w to vary as a constant (i.e. no dependence on z). The bottom-left panel of Fig. 10 presents the joint posterior probability of H_0 and w. Here, we see that the CMB alone does not constrain this combination well, showing a large allowed range towards the lower region of w. Adding the pre-reconstruction WiggleZ information does little to improve these measurements. Replacing with the post-reconstruction WiggleZ $D_{\rm V}(r_{\rm s}^{\rm fid}/r_{\rm s})$, we see a slight improvement of the w measurement on its low side of the 68 per cent confidence region (but there is no improvement on the high side). A further substantial improvement is achieved when adding information from the 6dFGS baryonic acoustic feature resulting in $w = -1.08^{+0.15}_{-0.12}$, an $\sim$13 per cent accuracy measurement. This can be explained by the fact that the low redshift $D_{\rm V}/r_{\rm s}$ is particularly sensitive to H_0, helping to break the degeneracy.

4.5.3 *o*Λ*CDM results*

When allowing for variation of $\Omega_{\rm K}$ and assuming $w = -1$, we notice some improvement in constraints when adding the WiggleZ pre-reconstruction to that of the CMB. When replacing the WiggleZ pre-reconstruction $A(z)$ by the post-reconstruction $D_{\rm V}(r_{\rm s}^{\rm fid}/r_{\rm s})$, however, we see substantial improvement in the measurements on the high side of $\Omega_{\rm K}$. Further improvement to measurements on the low side of $\Omega_{\rm K}$ are obtained when adding information from the 6dFGS baryonic acoustic feature. These are shown in the top-right panel of Fig. 10 which displays the joint posterior probability of H_0 and $\Omega_{\rm K}$.

[3] Note that this is generic because $i\sin(ix) = -\sinh(x)$.

Table 5. Constraints assuming flat ΛCDM.

Parameter/Data set(s)	CMB	CMB+(WiggleZ no-recon)	CMB+(WiggleZ w/recon)	CMB+(WiggleZ w/recon)+6dFGS
ΛCDM				
H_0	$67.26^{+1.19}_{-1.20}$	$67.52^{+1.05}_{-1.03}$	$67.00^{+1.02}_{-1.03}$	$67.15^{+0.99}_{-0.97}$
Ω_m	$0.316^{+0.016}_{-0.018}$	$0.312^{+0.014}_{-0.014}$	$0.319^{+0.014}_{-0.016}$	$0.317^{+0.013}_{-0.015}$
$-2\ln(L)$	9805.3	9805.2	9805.4	9804.9
wCDM				
H_0	$83.36^{+14.70}_{-7.29}$	$81.15^{+9.67}_{-11.60}$	$72.33^{+5.09}_{-10.48}$	$69.04^{+3.26}_{-4.01}$
Ω_m	$0.217^{+0.023}_{-0.078}$	$0.227^{+0.035}_{-0.074}$	$0.285^{+0.067}_{-0.059}$	$0.304^{+0.030}_{-0.033}$
w	$-1.49^{+0.25}_{-0.42}$	$-1.44^{+0.33}_{-0.34}$	$-1.18^{+0.36}_{-0.19}$	$-1.08^{+0.15}_{-0.12}$
ΔAIC	0.3	−0.1	−2.8	−2.6
oΛCDM				
H_0	$56.13^{+5.26}_{-6.05}$	$66.24^{+2.61}_{-2.60}$	$64.92^{+2.03}_{-2.05}$	$65.84^{+1.69}_{-1.70}$
Ω_m	$0.462^{+0.072}_{-0.107}$	$0.324^{+0.024}_{-0.028}$	$0.337^{+0.022}_{-0.024}$	$0.327^{+0.017}_{-0.019}$
$100\Omega_K$	$-3.83^{+2.91}_{-1.78}$	$-0.39^{+0.74}_{-0.66}$	$-0.64^{+0.62}_{-0.55}$	$-0.43^{+0.47}_{-0.47}$
ΔAIC	0.5	−2.5	0.0	−2.7
owCDM				
H_0	$61.24^{+9.28}_{-21.01}$	$80.26^{+9.41}_{-12.47}$	$76.40^{+7.29}_{-13.06}$	$70.38^{+3.43}_{-4.55}$
Ω_m	$0.451^{+0.119}_{-0.289}$	$0.230^{+0.037}_{-0.079}$	$0.255^{+0.057}_{-0.080}$	$0.289^{+0.032}_{-0.032}$
w	$-1.23^{+0.84}_{-0.47}$	$-1.55^{+0.44}_{-0.37}$	$-1.50^{+0.51}_{-0.33}$	$-1.27^{+0.24}_{-0.18}$
$100\Omega_K$	$-4.18^{+4.23}_{-1.55}$	$-0.54^{+0.46}_{-0.47}$	$-0.78^{+0.42}_{-0.43}$	$-0.83^{+0.44}_{-0.55}$
ΔAIC	−0.8	−1.5	−1.4	−2.4

CMB refers to temperature fluctuations of Planck Collaboration et al. (2013b) and *WMAP*9 polarization (Bennett et al. 2013).
WiggleZ no-recon refers to the pre-reconstruction $A(z)$ obtained by using the full shape of ξ (Blake et al. 2011).
WiggleZ w/recon refers to the post-reconstruction $D_V(r_s^{fid}/r_s)$ measurements presented here.
6dFGS refers to the baryonic acoustic feature measurements of that survey (Beutler et al. 2011).
In the ΛCDM section, we quote the maximum likelihood as $-2\ln L$.
In the *w*CDM, *o*ΛCDM, *ow*CDM sections, we quote the $\Delta\mathrm{AIC} \equiv \mathrm{AIC}_{\Lambda\mathrm{CDM}} - \mathrm{AIC}_{\mathrm{M}}$ of each model M, as explained in the text. A positive ΔAIC indicates a preference for the model M over ΛCDM and vice versa. The relative likelihood of the model M can be quantified as $\exp(\Delta\mathrm{AIC}/2)$.

4.5.4 ow*CDM results*

Lastly, we allow both w and Ω_K to vary and find results to be consistent with the flat cosmological constant paradigm. This is shown in the bottom-right panel of Fig. 10 which displays the joint posterior probability of these parameters. As expected, the CMB-only results do not constrain these parameters well, and the addition of the WiggleZ information yields substantial improvement. As noticed in the case of *o*ΛCDM case, we obtain a clear improvement in the higher end of the confidence region of Ω_K when adding to the CMB the reconstructed WiggleZ $D_V(r_s^{fid}/r_s)$, compared to adding the pre-reconstruction $A(z)$. The marginalized 68 per cent confidence region of Ω_K is limited to $[-0.0121, -0.0036]$.

Adding the baryonic acoustic feature from the 6dFGS does not improve constraints on the curvature but does substantially reduce the allowed space for w, as seen in the *w*CDM case. In the case of CMB+(WiggleZ post-recon)+6dFGS we obtain a marginalized result of $w = -1.27^{+0.24}_{-0.18}$, a 17 per cent accuracy measurement.

To better understand contributions from WiggleZ compared to those from 6dF, when added to the CMB information, in the bottom-right panel of Fig. 10 we plot in yellow dashed constraints obtained with CMB+6dF without WiggleZ data. This result shows that CMB+6dF alone is not enough to simultaneously constrain w and Ω_K. We do find in the *o*ΛCDM case, however, that CMB+6dF constrains H_0 and Ω_K in a similar manner to results obtained using CMB+(WiggleZ pre-recon).

As mentioned above, in all of our tests we find consistency with ΛCDM model. We now turn to quantify the model selection compared to ΛCDM. For this purpose, we use the Akaike information criterion, which incorporates trade-offs between the goodness of fits to the additional complexity of each model (Akaike 1974). For each model M we quantify $\mathrm{AIC}_M \equiv 2p - 2\ln(L)$, where p is the number of parameters and L is the maximized value of the likelihood function. We then define $\Delta\mathrm{AIC} \equiv \mathrm{AIC}_{\Lambda\mathrm{CDM}} - \mathrm{AIC}_M$ as our indicator of the preferred model. A positive ΔAIC prefers model M over ΛCDM and vice versa. The relative likelihood of the models can be quantified as $\exp(\Delta\mathrm{AIC}/2)$.

In Table 5, we list the ΔAIC of the models *w*CDM, *o*ΛCDM, *ow*CDM, which should be read by column (for each data set combination). We find non-positive values of ΔAIC values for all the data sets which include BAO in all models, meaning that the model that is preferred given the data (CMB, WiggleZ, 6dFGS) is ΛCDM. For example, when comparing the *w*CDM model to ΛCDM and using the CMB+(WiggleZ w/recon) we obtain $\Delta\mathrm{AIC} = -2.8$, i.e. the relative likelihood of the *w*CDM model is 0.247 times that of ΛCDM according to the Akaike information criteria.

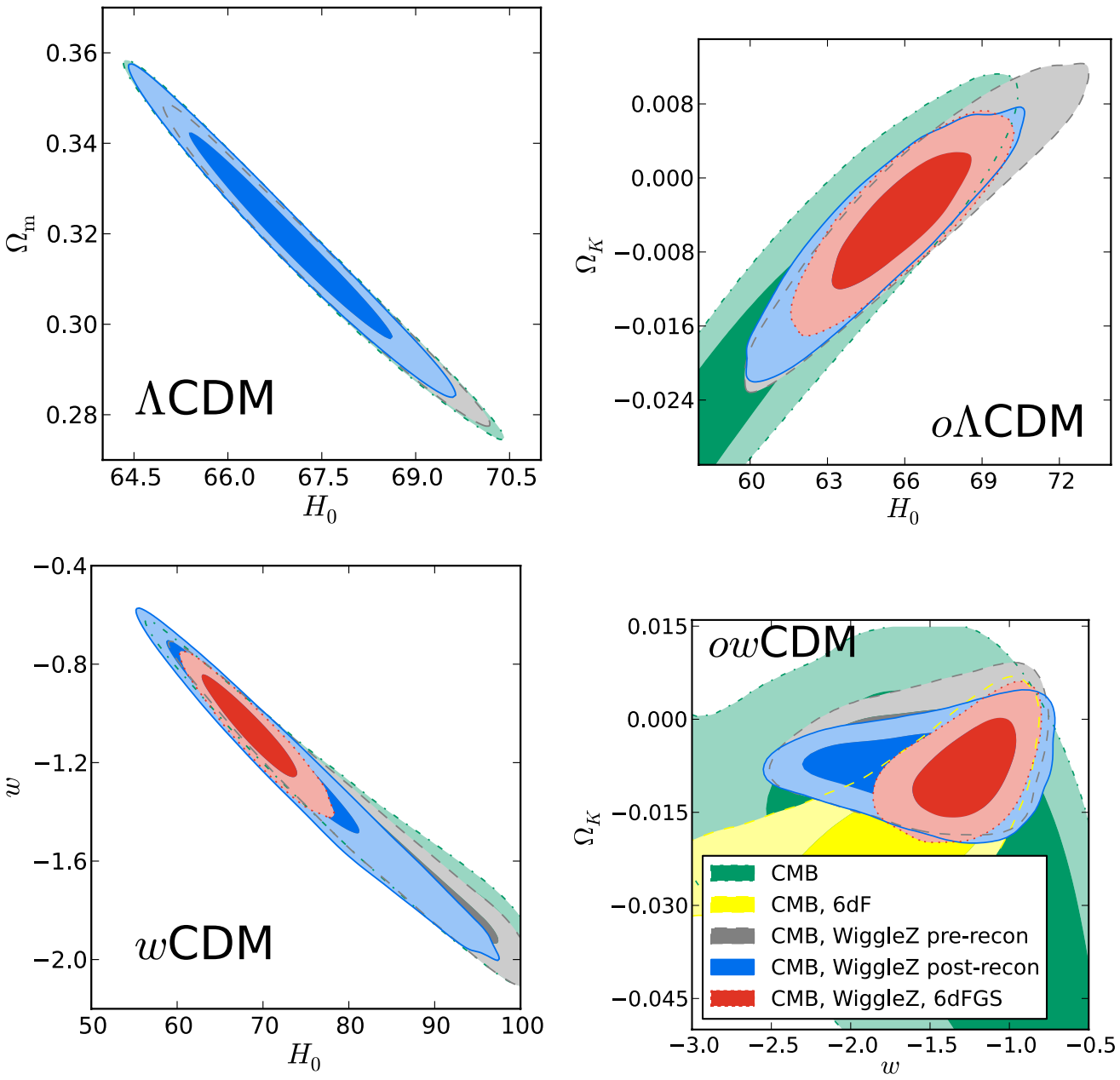

Figure 10. Marginalized 68 and 95 per cent joint confidence regions of cosmological parameter pairs, as indicated. In the left-hand panels, we assume flatness, where the top-left panel is ΛCDM and the bottom left is wCDM, where w is the equation of state of dark energy. In the right-hand panels, we let the curvature Ω_K vary, where the top-right panel is $o\Lambda$CDM and the bottom right is owCDM. The expansion rate H_0 is in units of km s^{-1} Mpc^{-1} and Ω_m is the matter density. In all panels, the dot–dashed green contours are when using information only from the CMB: *Planck* temperature fluctuations (Planck Collaboration et al. 2013b) and *WMAP*9 polarization (Bennett et al. 2013). CMB, WiggleZ pre-recon (dashed grey) is when adding $A(z)$ information from the WiggleZ ξ full-shape analysis (Blake et al. 2011). CMB, WiggleZ post-recon (solid blue) is when adding to CMB our post-reconstruction $D_V(r_s^{fid}/r_s)$ results. The CMB, WiggleZ, 6dFGS results (dotted red) is when we add to CMB, WiggleZ post-recon BAO results from the 6dFGS (Beutler et al. 2011). For comparison, in the bottom right we also show results of CMB+6dFGS without WiggleZ information.

5 SUMMARY

We present improved distance measurements in the redshift shift range $0.2 < z < 1$ using the WiggleZ Dark Energy Survey galaxies, by applying the reconstruction of the baryonic acoustic feature technique, which utilizes additional information encoded in the density field.

The constraints on $D_V(r_s^{fid}/r_s)$ are 1716 ± 83 Mpc, 2221 ± 101 Mpc, 2516 ± 86 Mpc (68 per cent CL) for effective redshifts $z_{eff} = 0.44, 0.6, 0.73$, respectively. These results are model independent as we focus on the geometrical information contained in the baryonic acoustic feature, and not the full shape of ξ.

Fig. 8 shows a comparison of WiggleZ D_V/r_s measurements obtained by various methods with other data sets and cosmological predictions. The D_V/r_s measurements obtained by analysis of the baryonic acoustic feature position when using pre- and post-reconstruction data are shown to be consistent. Furthermore, these

results also agree with those obtained by Blake et al. (2011), who used the full shape of the pre-reconstruction ξ as a standard ruler.

Interestingly, although we use a cosmology as predicted by *WMAP* as our fiducial, when converting redshifts to comoving distances before counting the pairs of galaxies, the post-reconstruction D_V/r_s results show a preference for the distance–redshift predictions of the best-fitting cosmologies measured by Planck Collaboration et al. (2013a) and BOSS (e.g. Sánchez et al. 2013).

These 3.4–4.8 per cent accuracy post-reconstruction D_V/r_s measurements represent a significant improvement from the pre-reconstruction case, and from the analysis of the full shape of ξ.[4] These measurement improvements are effectively equivalent to those expected from surveys with up to 2.5 times the volume of WiggleZ.[5] To be conservative, here we assume a comparison between our post-reconstruction BAO-only results to those of the pre-reconstruction ξ full-shape analysis reported by Blake et al. (2011).[6]

We test for sample variance by analysing 600 mock simulations and find that reconstruction of the density field should yield a sharpened baryonic acoustic feature 65 per cent of the time, and our $D_V(r_s^{fid}/r_s)$ results are within these expectations.

The main limitations of the WiggleZ combined volumes are the edge effects, completeness and large shot-noise. Although we show that reconstruction successfully works on the data and most mocks, we find that it fails to yield an improved significance of detection of the baryonic acoustic feature in ∼30–40 per cent of the cases, depending on the redshift range. We also find that 3–6 per cent of the mock realizations fail to detect a baryonic acoustic feature post-reconstruction.

In Table 4, we provide the inverse covariance matrix of the $D_V(r_s^{fid}/r_s)$ measurements between these overlapping Δz volumes, which can be used to calculate cosmological implications. We combine our measurements with CMB temperature anisotropies from *Planck* and CMB polarization of *WMAP*9, as well as the baryonic acoustic feature of the 6dFGS.

Using these post-reconstruction $D_V(r_s^{fid}/r_s)$ measurements, we obtain consistent measurements of fundamental cosmological parameters compared with those obtained when using the Blake et al. (2011) $A(z)$ results. Assuming a curved CDM model while varying the equation of state of dark energy, we find consistency with the flat ΛCDM model. The significant improvement in measuring $D_V(r_s^{fid}/r_s)$, obtained by applying reconstruction, yields moderate improvements on constraining Ω_K ($o\Lambda$CDM, owCDM), and only slight improvement in w (wCDM, owCDM) and H_0, Ω_m (when examining the flat ΛCDM model).

Testing the ΛCDM model we obtain a marginalized constraint of $H_0 = 67.15 \pm 0.98$ km s^{-1} Mpc^{-1}, which is in a 2.6σ tension with the SH0ES measurement of $H_0 = 73.8 \pm 2.4$ km s^{-1} Mpc (Riess et al. 2011).[7] The density of matter is constrained in the range $\Omega_m = 0.317 \pm 0.014$. Relaxing the assumption of flatness we constrain the curvature to $\Omega_K = -0.0043 \pm 0.0047$. When assuming a flat wCDM model, the equation of state of dark energy is estimated to be $w_{DE} = -1.08 \pm 0.135$.

In the analysis of the cosmological constraints, we do not compare results with those of the SDSS. Although the overlap between the surveys is small, current investigation is underway to quantify the covariance of the D_V/r_s measurements of the surveys (Beutler, Blake et al. in preparation).

To summarize we find that, although the reconstruction procedure is most effective in contiguous surveys, it can be applied successfully in surveys that are patchy, that have high shot-noise and significant edge effects. This demonstrates the power of the technique in producing a sharper baryonic acoustic feature from which we can obtain significantly improved unbiased distance measurements.

[4] This statement is true for our analysis in the context of constraining D_V/r_s; the full shape of ξ contains more information, e.g. $\Omega_m h^2$ and n_s, which is not investigated here.

[5] The calculation is based on squaring the uncertainty ratio, where we assume $\sigma_\alpha^2 \propto 1/\text{Volume}$.

[6] When comparing between BAO-only pre- and post-reconstruction the improvement is effectively equivalent to surveys with volumes up to 4.7 larger than WiggleZ.

[7] Calculation: $(73.8-67.15)/\sqrt{2.4^2+0.98^2} = 2.6$

ACKNOWLEDGEMENTS

We thank Florian Beutler, Daniel Eisenstein, Shahab Joudaki, Antony Lewis, Felipe Marin and Ariel Sanchez for useful discussions. EK and JK are supported by the Australian Research Council Centre of Excellence for All-sky Astrophysics (CAASTRO), through project number CE110001020. CB acknowledges the support of the Australian Research Council through the award of a Future Fellowship. TMD acknowledges the support of the Australian Research Council through a Future Fellowship award, FT100100595. The numerical simulation was supported by the SwinSTAR supercomputer at Swinburne University of Technology and the Raijin supercomputer through the Flagship Allocation Scheme of the NCI National Facility at the ANU.

REFERENCES

Akaike H., 1974, Ann. Stat., 19, 461
Anderson L. et al., 2012, MNRAS, 427, 3435
Anderson L. et al., 2014a, MNRAS, 441, 24
Anderson L. et al., 2014b, MNRAS, 439, 83
Angulo R. E., Baugh C. M., Frenk C. S., Lacey C. G., 2008, MNRAS, 383, 755
Bennett C. L. et al., 2013, ApJS, 208, 20
Bernardeau F., Colombi S., Gaztañaga E., Scoccimarro R., 2002, Phys. Rep., 367, 1
Beutler F. et al., 2011, MNRAS, 416, 3017
Blake C., Glazebrook K., 2003, ApJ, 594, 665
Blake C. et al., 2011, MNRAS, 418, 1707
Blake C. et al., 2012, MNRAS, 425, 405
Carlson J., White M., 2010, ApJS, 190, 311
Crocce M., Scoccimarro R., 2008, Phys. Rev. D, 77, 023533
Drinkwater M. J. et al., 2010, MNRAS, 401, 1429
Eisenstein D. J., Hu W., 1998, ApJ, 496, 605
Eisenstein D. J. et al., 2001, AJ, 122, 2267
Eisenstein D. J. et al., 2005, ApJ, 633, 560
Eisenstein D. J., Seo H.-J., Sirko E., Spergel D. N., 2007, ApJ, 664, 675
Feldman H. A., Kaiser N., Peacock J. A., 1994, ApJ, 426, 23
Hartlap J., Simon P., Schneider P., 2007, A&A, 464, 399
Hoffman Y., Ribak E., 1991, ApJ, 380, L5
Hogg D. W., 1999, preprint (astro-ph/9905116)
Kazin E. A., Sánchez A. G., Blanton M. R., 2012, MNRAS, 419, 3223
Kazin E. A. et al., 2013, MNRAS, 435, 64
Kim J., Park C., Gott J. R., III, Dubinski J., 2009, ApJ, 701, 1547
Komatsu E. et al., 2009, ApJS, 180, 330
Landy S. D., Szalay A. S., 1993, ApJ, 412, 64
Lewis A., Challinor A., Lasenby A., 2000, Astrophys. J., 538, 473
Lewis I. et al., 2002, MNRAS, 334, 673
Manera M. et al., 2013, MNRAS, 428, 1036
Mehta K. T., Seo H.-J., Eckel J., Eisenstein D. J., Metchnik M., Pinto P., Xu X., 2011, ApJ, 734, 94

Mehta K. T., Cuesta A. J., Xu X., Eisenstein D. J., Padmanabhan N., 2012, MNRAS, 427, 2168
Meiksin A., White M., Peacock J. A., 1999, MNRAS, 304, 851
Noh Y., White M., Padmanabhan N., 2009, Phys. Rev. D, 80, 123501
Padmanabhan N., White M., Cohn J. D., 2009, Phys. Rev. D, 79, 63523
Padmanabhan N., Xu X., Eisenstein D. J., Scalzo R., Cuesta A. J., Mehta K. T., Kazin E., 2012, MNRAS, 427, 2132
Peebles P. J. E., Yu J. T., 1970, ApJ, 162, 815
Percival W. J. et al., 2002, MNRAS, 337, 1068
Perlmutter S. et al., 1999, ApJ, 517, 565
Planck Collaboration et al., 2013a, preprint (arXiv:1303.5076P)
Planck Collaboration et al., 2013b, preprint (arXiv:1303.5075P)
Riess A. G. et al., 1998, AJ, 116, 1009
Riess A. G. et al., 2011, ApJ, 730, 119
Sánchez A. G., Baugh C. M., Angulo R., 2008, MNRAS, 390, 1470
Sánchez A. G., Crocce M., Cabré A., Baugh C. M., Gaztañaga E., 2009, MNRAS, 400, 1643
Sánchez A. G. et al., 2012, MNRAS, 425, 415
Sánchez A. G. et al., 2013, MNRAS, 433, 1202
Sanchez A. G. et al., 2014, MNRAS, 440, 2692
Seo H.-J., Eisenstein D. J., 2003, ApJ, 598, 720
Seo H.-J., Eisenstein D. J., 2007, ApJ, 665, 14
Seo H.-J., Siegel E. R., Eisenstein D. J., White M., 2008, AJ, 686, 13
Seo H. et al., 2010, ApJ, 720, 1650
Smith R. E., Scoccimarro R., Sheth R. K., 2008, Phys. Rev. D, 77, 043525
Taruya A., Saito S., Nishimichi T., 2011, Phys. Rev. D, 83, 103527
Tassev S., Zaldarriaga M., Eisenstein D. J., 2013, J. Cosmol. Astropart. Phys., 6, 36
White M. et al., 2011, ApJ, 728, 126
Xu X., Padmanabhan N., Eisenstein D. J., Mehta K. T., Cuesta A. J., 2012, MNRAS, 427, 2146
York D. G. et al., 2000, AJ, 120, 1579
Zel'dovich Y. B., 1970, A&A, 5, 84

[1]*Centre for Astrophysics and Supercomputing, Swinburne University of Technology, PO Box 218, Hawthorn, VIC 3122, Australia*
[2]*ARC Centre of Excellence for All-sky Astrophysics (CAASTRO), 44 Rosehill Street, Redfern, NSW 2016, Australia*
[3]*Department of Physics, Yale University, 260 Whitney Ave, New Haven, CT 06520, USA*
[4]*Australian Astronomical Observatory, PO Box 915, North Ryde, NSW 1670, Australia*
[5]*Carnegie Institution of Washington, Las Campanas Observatory, Colina el Pino s/n, Casilla 601, Chile*
[6]*Sydney Institute for Astronomy, School of Physics, University of Sydney, NSW 2006, Australia*
[7]*School of Mathematics and Physics, University of Queensland, Brisbane, QLD 4072, Australia*
[8]*California Institute of Technology, MC 278-17, 1200 East California Boulevard, Pasadena, CA 91125, USA*
[9]*South African Astronomical Observatory, PO Box 9, Observatory 7935, South Africa*
[10]*Department of Astronomy and Astrophysics, University of Chicago, 5640 South Ellis Avenue, Chicago, IL 60637, USA*
[11]*Australia Telescope National Facility, CSIRO, Epping, NSW 1710, Australia*
[12]*Department of Astronomy and Astrophysics, University of Toronto, 50 St George Street, Toronto, ON M5S 3H4, Canada*
[13]*Observatories of the Carnegie Institute of Washington, 813 Santa Barbara St, Pasadena, CA 91101, USA*
[14]*School of Physics, Monash University, Clayton, VIC 3800, Australia*
[15]*Department of Physics and Mathematics, University of Hull, Cottingham Road, Hull HU6 7RX, UK*
[16]*School of Physics, University of Melbourne, Parksville, VIC 3010, Australia*
[17]*Research School of Astronomy and Astrophysics, Australian National University, Weston Creek, ACT 2600, Australia*
[18]*Max Planck Institut für extraterrestrische Physik, Giessenbachstraβe, D-85748 Garching, Germany*
[19]*Department of Physics and Astronomy, University of British Columbia, 6224 Agricultural Road, Vancouver, BC V6T 1Z1, Canada*

This paper has been typeset from a TEX/LATEX file prepared by the author.